Perspectives of a Midrapidity Dimuon Program at RHIC: A Novel and Compact Muon Telescope Detector

L. Ruan, Z. Xu, K. Asselta, W. Christie, C. D'Agostino, J. Dunlop, J. Scheblein, R. Soja, A.H. Tang, T. Ullrich
Brookhaven National Laboratory, Upton, New York 11973

H.J. Crawford, J. Engelage
University of California, Berkeley, California 94720

M. Calderón de la Barca Sánchez, R. Reed, H.D. Liu
University of California, Davis, California 95616

G. Eppley, F. Geurts, J. Liu, W.J. Llope, D. McDonald, T. Nussbaum, J. Roberts, L. Bridges
Rice University, Houston, Texas 77251

H.F. Chen, B.C. Huang, C. Li, M. Shao, Y.J. Sun, Z.B. Tang, X.L. Wang, Y.C. Xu, Z.P. Zhang, H. Zeng, Y. Zhou
University of Science & Technology of China, Hefei 230026, China

R. Clarke, S. Mioduszewski
Texas A&M University, College Station, Texas 77843

A. Davila, G.W. Hoffmann, L. Li, C. Markert, L. Ray, J. Schambach, D. Thein, M. Wada
University of Texas, Austin, Texas 78712

J.P. Chen, K.J. Kang, Y.J. Li, Y. Wang, X.L. Zhu
Tsinghua University, Beijing 100084, China

Z. Ahammed, P.P. Bhaduri, S. Chattopadhyay, A.K. Dubey, M.R. Dutt-Mazumdar, P. Ghosh, S.A. Khan, S. Muhuri,

B. Mohanty, T.K. Nayak, S. Pal, R. Singaraju, V. Singhal, P. Tribedy, Y.P. Viyogi

Variable Energy Cyclotron Centre, Kolkata 700064, India

PACS numbers: 25.75.Cj, 29.40.Cs

1. Executive Summary

We propose a large-area and cost-effective Muon Telescope Detector (MTD) at mid-rapidity for the Solenoidal Tracker at RHIC (STAR) at Brookhaven National Laboratory. A novel muon detector utilizing the new Time-of-Flight (TOF) system with precise timing and hit position is different from the conventional muon detector, consisting of a sandwich of tracking stations, trigger detectors, and absorbers, in high-energy particle and nuclear physics experiments. The proposed large-area MTD covers $\sim 45\%$ in azimuth and $|\eta| < 0.5$ in pseudorapidity, behind the return iron bars for the STAR magnetic. It will provide excellent muon trigger and identification capabilities at mid-rapidity in the high-luminosity era at RHIC. The project will be a joint effort by two institutions from China (USTC and Tsinghua University) funded by NNSFC, one institution from India (VECC), and several institutes from the United States (BNL, UC Berkeley, UC Davis, Rice, UT Austin, and Texas A&M) funded by DOE and NSF. The project responsibilities will be similar to that of the TOF project. The Chinese and Indian institutions will fabricate the long MRPC modules, while the US institutions are responsible for the electronics, the assembly of the trays, and the operation of the detector. We propose to start the project in FY2011 and complete the project in FY2013.

The MTD will directly address many of the open questions and long-term goals during the RHIC-II era by advancing our knowledge of Quark Gluon Plasma (QGP) properties. Among many exciting perspectives, we will be able to collect a large sample of J/ψ events, to separate different Upsilon states with a clear advantage over electron decay channels due to the reduced Bremsstrahlung radiation and Dalitz decay background, and to provide a unique measurement of $\mu - e$ correlations from heavy-flavor decays. The funding will mainly be devoted to the detector construction, electronics fabrication, and personnel support for the project. We will be able to take advantage of the experience and infrastructure from the newly installed TOF system in STAR, and retain the engineering resources to build the electronics and detector trays. We have performed research and development (R&D) to demonstrate the feasibility of this detector and published the results in the Journal of Physics G: Nucl. Part. Phys. 36 (2009) 095001 [1] and Nucl. Instrum. Methods A 593 (2008) 307. The R&D project was partly supported by the BNL Laboratory Director R&D (BNL LDRD07-007). We utilized Multi-gap Resistive Plate Chambers with long readout strips ("LMRPCs") in the detector design. The results from cosmic ray and beam tests show that the intrinsic timing and the spatial resolution for a LMRPC are sufficient for the MTD requirements. The performance of the prototype muon telescope detector installed

in STAR demonstrates that clean muon identification at a transverse momentum of a few GeV/c can be achieved. This provides a promising device for future quarkonia studies and primordial dilepton measurements at RHIC.

2. Introduction

Data taken over the last several years have demonstrated that RHIC has created dense and rapidly thermalizing matter characterized by: 1) initial energy densities far above the critical values predicted by lattice QCD for formation of a Quark-Gluon Plasma (QGP); 2) opacity to jets; and 3) nearly ideal fluid flow, which is marked by constituent interactions of very short mean free path, established most probably at a stage preceding hadron formation [2]. The next objective at RHIC is to study properties of this partonic matter in detail in terms of color degrees of freedom and the equation of state. For example, due to color screening, different quarkonium states will dissociate, and the dissociation temperatures will be different due to different binding energies. The precise measurement of transverse momentum distributions of quarkonia at different centralities, collision systems, and energies will serve as a thermometer of the QGP. A large-area Muon Telescope Detector (MTD) at mid-rapidity for RHIC collisions will be crucial for advancing our knowledge of QGP properties. It will directly address many of the open questions and long-term goals proposed in the RHIC white papers [2, 3]. Since muons do not participate in strong interactions, they provide penetrating probes for the strongly interacting QGP. A large area detector identifying muons with momentum of a few GeV/c at mid-rapidity allows for the detection of di-muon pairs from QGP thermal radiation, quarkonia, light vector mesons, possible correlations of quarks and gluons as resonances in the QGP, and Drell-Yan production, as well as the measurement of heavy flavor hadrons through their semi-leptonic decays into single muons [4, 5]. Some of these topics also can be studied using electrons or photons or a combination of both. However, electrons and photons have large backgrounds from hadron decays, π^0 and η Dalitz decays, and gamma conversions in the detector material. These backgrounds prevent effective triggering in central nucleus-nucleus collisions at mid-rapidity in the Solenoidal Tracker at RHIC (STAR). In addition, electron-muon correlations can be used to distinguish between lepton pair production and heavy quark decays ($c+\bar{c} \rightarrow e+\mu(e)$, $B \rightarrow e(\mu)+c \rightarrow e+\mu(e)$). In addition, muons are less affected by Bremsstrahlung radiation energy loss in the detector material than electrons, thus providing excellent mass resolution of vector mesons and quarkonia. This is essential for separating the ground state (1S) of the Υ from its excited states (2S+3S). They are predicted to melt at very different temperatures.

Conventional muon detectors rely heavily on tracking stations, while this new detector proposes to use <100 ps timing and ∼1 cm spatial resolution to identify muons with momentum of a few GeV/c [6]. Multi-gap resistive plate chamber technology with large modules, long strips, and double-ended readout ("LMRPC") was used for MTD prototype detectors. Similar technology but with small pads has been constructed and installed at STAR as a Time-of-Flight Detector (TOF) [7]. In this report we present the conceptual

design for the STAR MTD, the R&D results including the intrinsic timing and spatial resolution of an LMRPC, and the MTD prototype performance at STAR. The muon identification capability and hadron background rejection are reported. Future perspectives for physics programs utilizing such detectors are discussed.

3. Physics Cases

The MTD can provide crucial measurements for many exciting physics perspectives as mentioned in the introduction and in the RHIC experimental white papers summarizing the accomplishments in the first three years [2, 3] and the RHIC II papers on future measurements [4, 5, 8]. In this section, we elaborate on a few of the physics cases to which the MTD will make important contributions.

3.1. Quarkonium Dissociation at high p_T

Suppression of the $c\bar{c}$ bound state J/ψ meson production in relativistic heavy-ion collisions arising from J/ψ dissociation due to screening of the $c\bar{c}$ binding potential in the deconfined medium has been proposed as a signature of QGP formation [9]. Measurements at $\sqrt{s_{\rm NN}}$ = 17.3 GeV at the CERN-SPS observed a strong suppression of J/ψ production in heavy-ion collisions [10], although the magnitude of the suppression decreases with increasing J/ψ p_T. This systematic dependence may be explained by initial state scattering (Cronin effect [11, 12]), as well as the combined effects of finite J/ψ formation time and the finite space-time extent of the hot, dense volume where the dissociation can occur [13].

At higher beam energy ($\sqrt{s_{\rm NN}}$ = 200 GeV), the PHENIX collaboration at RHIC has measured J/ψ suppression for $p_T < 5$ GeV/c in central Au+Au and Cu+Cu collisions [14] that is similar in magnitude to that observed at the CERN-SPS. This similarity is surprising in light of the expectation that the energy density is significantly higher at larger collision energy. It may be due to the cold nuclear absorption and the counterbalancing of larger dissociation with recombination of unassociated c and $\bar{c}$ in the medium, which are more abundant at higher energy [15, 16, 17, 18] (for a recent review see [8]).

The medium generated in RHIC heavy-ion collisions is thought to be strongly coupled [2], making accurate QCD calculations of quarkonium propagation difficult. The AdS/CFT duality for QCD-like theories may provide insight into heavy fermion pair propagation in a strongly coupled liquid. One such calculation predicts that the dissociation temperature decreases with increasing J/ψ p_T (or velocity) [19]. The temperature achieved at RHIC ($\sim$1.5 T_c) [2] is below this dissociation temperature at low J/ψ p_T, and above it at $p_T \gtrsim 5$ GeV/c. Consequently, J/ψ production is predicted to be more suppressed at high p_T, in contrast to the standard suppression mechanism. This prediction can be tested with measurements of J/ψ over a broad kinematic range, in both p+p and nuclear collisions.

The nuclear modification factor $R_{AA}(p_T)$ [20] is defined as the ratio of the inclusive hadron yield in nuclear collisions to that in p+p collisions scaled by the underlying number

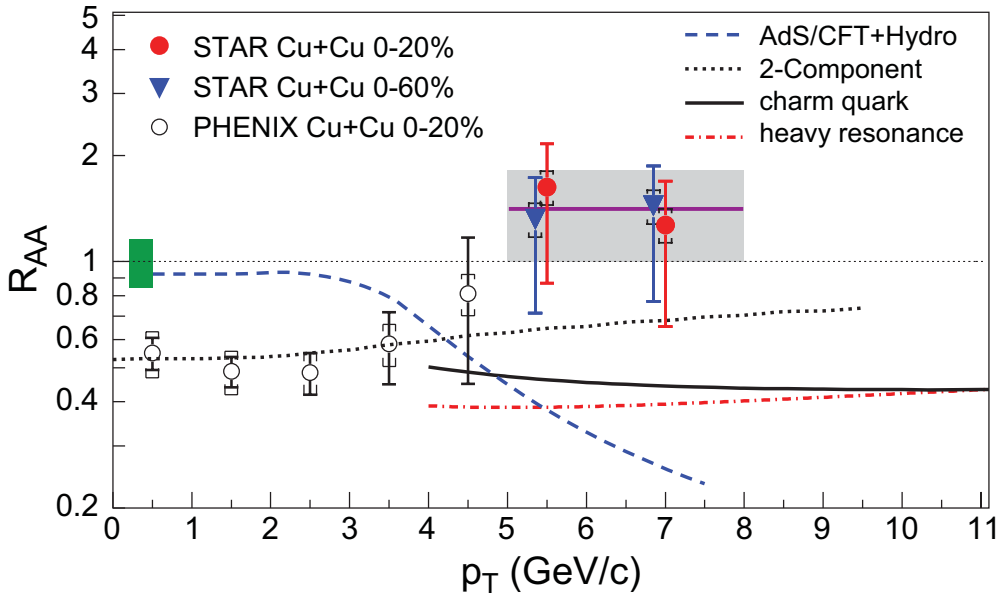

Figure 1. J/ψ R_{AA} vs. p_T. STAR data points have statistical (bars) and systematic (caps) uncertainties. The box about unity on the left shows R_{AA} normalization uncertainty, which is the quadrature sum of p+p normalization and binary collision scaling uncertainties. The solid line and band show the average and uncertainty of the two 0-20% data points. The curves are model calculations described in the text. The uncertainty band of 10% for the dotted curve is not shown.

of binary nucleon-nucleon collisions. It measures medium-induced effects on inclusive particle production. In the absence of such effects, R_{AA} is unity for hard processes. Figure 1 shows R_{AA} for J/ψ versus p_T, in the 0-20% most central Cu+Cu collisions from PHENIX [21] and STAR, and the 0-60% most central Cu+Cu collisions from STAR. The Cu+Cu and p+p data with $p_T > 5$ GeV/c are from STAR. The R_{AA} systematic uncertainty takes into account the correlated efficiencies of the Cu+Cu and p+p data sets. R_{AA} for J/ψ is seen to increase with increasing p_T. The average of the two STAR 0-20% data points at high-p_T is $R_{AA} = 1.4 \pm 0.4$ (stat.) $\pm$ 0.2 (syst.). Utilizing the STAR Cu+Cu and p+p data reported here and PHENIX Cu+Cu data at high-p_T [21] gives $R_{AA} = 1.1 \pm 0.3$ (stat.) ± 0.2 (syst.) for $p_T > 5$ GeV/c. Both results are consistent with unity and differ by two standard deviations from a PHENIX measurement at lower p_T ($R_{AA} = 0.52 \pm 0.05$ [21]).

The p+p data presented here enable the measurement of R_{AA} at substantially higher p_T than that accessible from previous data [22]. A value of $R_{AA} < 0.6$ for $p_T > 5$ GeV/c is excluded at the 97% confidence level. The enhanced p_T range from our data allows comparison to a calculation based on AdS/CFT+hydrodynamics [23], whose prediction is excluded at the 99% confidence level. A notable conclusion from these data is that J/ψ is the only hadron measured in RHIC heavy-ion collisions that does not exhibit significant high p_T suppression.

There are a few possible explanations for the observed effect.

- The observation suggests that high-p_T J/ψ production does not seem to proceed dominantly via a channel carrying color. If the nuclear modification factor were less than one, it could be due partonic energy loss in dense matter, where the J/ψ formation would then likely proceed through a channel carrying color.
- The J/ψ has a significant formation time during which it is not affected by the medium. If the medium generated in RHIC heavy-ion collisions is thought to be strongly coupled, the AdS/CFT duality for QCD-like theories calculating heavy fermion pair propagation in a strongly coupled liquid suggest that J/ψ production will be more suppressed at high p_T [19], in contrast to the standard suppression mechanism. However, the calculation shown in Figure 1 requires that the J/ψ be produced as an on-shell J/ψ fermion almost instantaneously at the initial impact with no formation time.
- The hot and dense medium created by Cu+Cu collisions is not thermalized and doesn't have large enough volume for the effect to take place. The larger system produced in Au+Au collisions may be necessary to observe or exclude the effect predicted by AdS/CFT [19].
- A calculation combining effects of suppression and regeneration can describe the observed trend. The "two-component" model, which includes color screening, hadronic phase dissociation, statistical c-$\bar{\text{c}}$ coalescence at the hadronic transition, J/ψ formation time effects, and B-meson feed-down, suggests a slight increase in the nuclear modification factor at higher transverse momenta [11].

The MTD will provide high efficiency, large acceptance, and effective triggering for $J/\psi \rightarrow \mu^+\mu^-$. Detailed simulations with realistic MTD detector effects are presented in the later section 4. In addition, correlations with hadrons or displaced vertices from the upgraded Heavy-Flavor Tracker will provide precise measurements of $B \rightarrow J/\psi + X$.

3.2. Dissociation of Υ *states*

Besides J/ψ, other quarkonium states are also suitable to study the effect of color screening in hot and dense QCD matter. Table 1 lists the available quarkonia and their dissociation temperatures. The Υ states are also ideal tools for this study since its ground states and excited states melt at different temperatures and all of them decay to dileptons. Furthermore, since the $b\bar{b}$ cross section at RHIC energy is expected to be much smaller compared to $c\bar{c}$ cross section from FONLL calculations [24], the recombination contribution from QGP phase might be negligible to bottomonia production. This makes the Υ even a better probe for studying the color screening effect in QGP if sufficient statistics can be achieved experimentally. However, with Bremsstrahlung radiation of electrons traversing the detector material, STAR is at the borderline of being able to separate the three states. The muons in $\Upsilon \rightarrow \mu^+\mu^-$ do not suffer from this degradation and we can cleanly separate the ground state from the excited states even with the upgraded inner tracker with additional material.

Detailed simulation studies are presented in the next section. In the RHIC-II era, with the full MTD system at STAR, we will be able to measure different Υ states with good precision by taking advantage of the high luminosity. This measurement will provide direct information on the temperature of QGP. Furthermore, the Upsilon measurement will be very helpful to understand quarkonia production mechanisms in hadron-hadron collisions.

Table 1. Quarkonium dissociation temperatures [25], illustrating the effects of binding energy on the dissociation temperature.

State	$J/\psi(1S)$	$\chi_c(1P)$	$\psi'(2S)$	$\Upsilon(1S)$	$\chi_b(1P)$	$\Upsilon(2S)$	$\chi_b(2P)$	$\Upsilon(3S)$
T_d/T_c	2.10	1.16	1.12	> 4.10	< 1.76	1.60	1.19	1.17

3.3. Dilepton measurements

The dilepton spectra at intermediate mass range (IMR) directly relate to the thermal radiation of the QGP [4, 5]. The relative QGP to four-pion yields in the IMR is essentially determined by the choice of T_c in the fireball evolution [26]: QGP dominates the IMR if $T_c = 160$ MeV while hadronic contributions are dominant if $T_c = 175$ MeV. Irrespective of whether the source is of QGP or hadronic origin, the IMR enhancement is associated with matter at temperatures close to T_c. The robustness of this conclusion is again a consequence of "parton-hadron duality" in the underlying emission rates.

Additional information on the nature of the emitting source might be obtained from quantitative analysis of dilepton q_t spectra, including elliptic flow. Such analysis has become possible with the NA60 data [27, 28]. Effective inverse slope parameters, $T_{\rm eff}$, have been extracted from dilepton excess spectra in the momentum range $0.4 < q_t < 1.8$ GeV, obtained from inclusive In+In collisions at the SPS with $dN_{\rm ch}/dy > 30$. Figure 2 shows the inverse slope parameter $T_{\rm eff}$ vs. dimuon mass for the combined LMR/IMR regions of the excess in comparison to hadrons. The extracted values of $T_{\rm eff}$ appear quite large relative to the hadronic slopes at freezeout, requiring a surprisingly strong collective flow for the moderate system size at SPS energies. The maximum $T_{\rm eff}(M)$, in the free ρ mass region, is indicative of ρ decays in the late stages of the collision where the line shape is expected to approach the vacuum shape, while the effective temperature, $T_{\rm eff} \simeq T_{\rm fo} + m\bar{v}^2$, is primarily due to the blue shift imprinted by the collective expansion velocity, $\bar{v}$. Note that the slope of the excess radiation at $M = m_{\rho,\omega}$ is larger than that of the ω (lower circle at $M = m_{\rho,\omega}$, suggesting that the ρ freezes out significantly later than the η, ω, and ϕ. In the IMR, $T_{\rm eff}$ is significantly reduced, in agreement with thermal emission early in the evolution, from temperatures close to T_c where the flow has not yet developed much, implying a small blue shift.

It would be very valuable to obtain similar information for Au+Au collisions at RHIC. The thermal yield is expected to dominate further, contributing at higher momenta, due to the larger system size and collision energy. (The multiplicity, $dN_{\rm ch}/dy$ in Au+Au collisions at RHIC is about a factor of four larger than that of In+In collisions at the

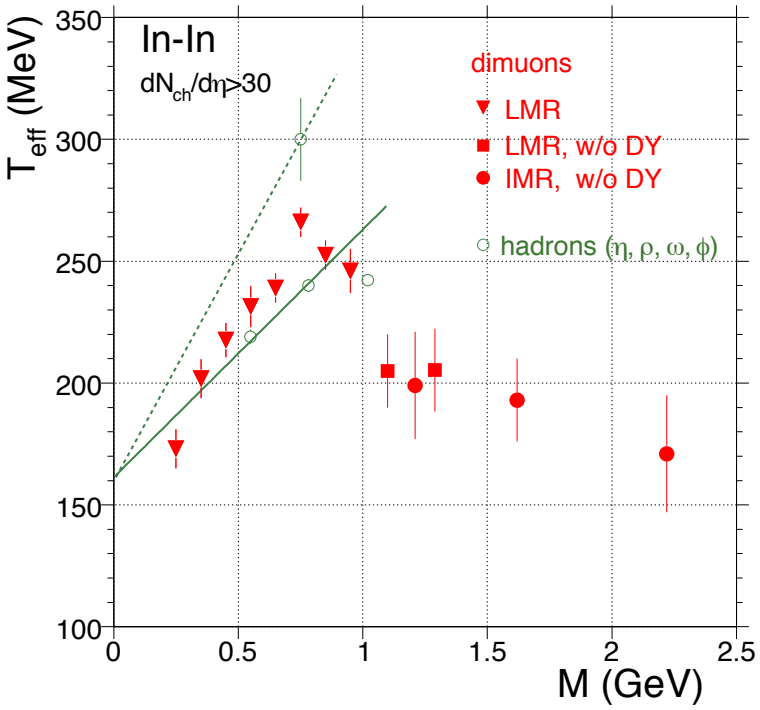

Figure 2. Inverse slope parameter $T_{\rm eff}$ vs. dimuon mass for the combined LMR/IMR regions of the excess in comparison to hadrons. Figure is taken from [27].

SPS.) Unfortunately, the increased contribution from correlated charm decays is sensitive not only to the total charm cross section but also to the charm momentum spectra and thus to charm thermalization (at low and intermediate p_T) and energy loss (at high p_T). Although the upgraded inner tracker (HFT) will provide a precise measurement of charm spectra and elliptic flow, a measurement of the correlation of $c\bar{c}$ is still challenging if not impossible. The MTD in STAR will provide $\mu-e$ correlation for the much needed independent measurements of heavy-flavor contribution to the dileptons.

4. Simulations

4.1. Monte Carlo Simulations of Muon Identification

The STAR detector was used for these studies [29]. The detector layout is shown in Fig. 3. The main tracking device is the Time Projection Chamber (TPC) [30], whose inner and outer field cages are located at radial distances of 50 and 200 cm respectively from the beam axis. The TPC is 4 meters long and it covers a pseudorapidity range $|\eta|<1.8$ and 2π in azimuth. The ionization energy loss (dE/dx) is used for particle identification [31, 32, 33]. A TOF detector based on Multi-gap Resistive Plate Chambers (MRPC) [34] was fully installed in STAR in 2009, covering 2π in azimuth and $-1<\eta<1$ in pseudorapidity at a radius of $\sim$220 cm. It will extend particle identification up to $p_T \sim 3$ GeV/c for p and $\bar{p}$ [35]. The

full barrel electromagnetic calorimeter (BEMC) is installed outside the TOF radius and uniformly covers -1<η<1 in pseudorapidity and 2π in azimuth [36]. The TPC is centered in a solenoidal magnetic field provided by the surrounding magnetic coils. The return flux path for the field is provided by the magnet steel [37], which is roughly cylindrical in geometry and consists of 30 flux return bars, four end rings, and two pole tips. The 6.85 m long flux return bars are trapezoidal in cross-section and 60 cm thick with a 363 cm outer radius. The width at the outer radius of the return bar is 57 cm.

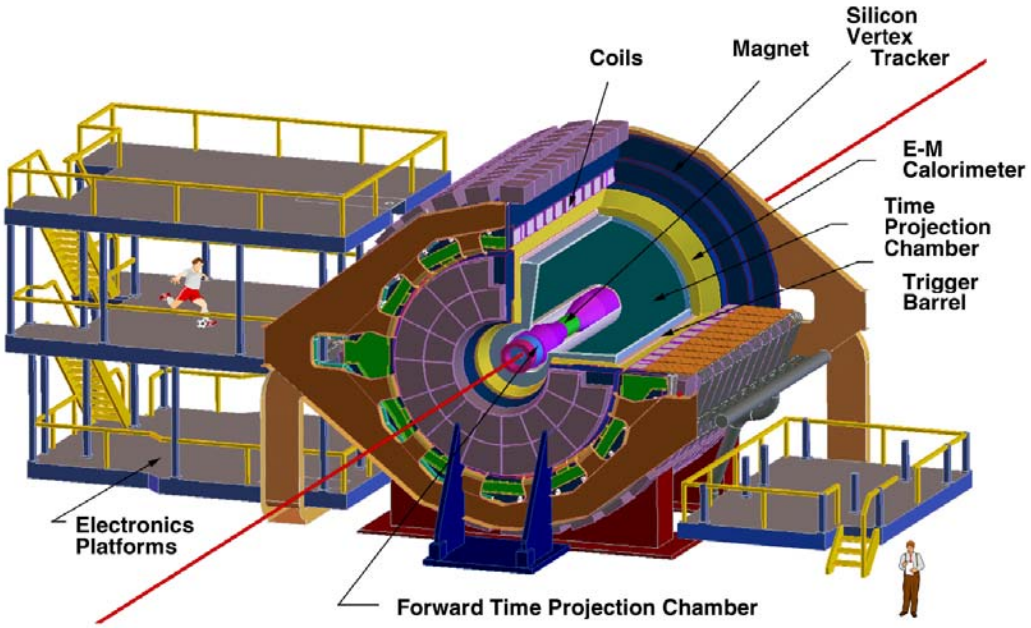

Figure 3. Perspective view of the STAR detector, with a cutaway for viewing inner detector systems. The trigger barrel, shown in this figure, will be fully replaced by the TOF detector in year 2009. Figure is taken from [29].

The simulation of a full HIJING central Au+Au collision is shown in Fig. 4, using STAR geometry with a configuration of all the detectors and a complete material budget. We simulated a muon-detector (in blue) covering the full return bars (in green) within $|\eta|$<0.8 and left the gaps in between the return bars uncovered. This detector acceptance corresponds to 56% of 2π in azimuth. In Fig. 4, it can be seen that most of the particles are stopped before the BEMC and the few escaping particles (primary or secondary) mainly come through the gaps between the return bars.

Further simulations [38] with the STAR geometry indicate that for a muon with p_T>2 GeV/c generated in the center of the TPC, the detection efficiency of the MTD, including acceptance effects, is about 40-50%, while for a pion track, the efficiency is 0.5-1%. In this simulation, the charged tracks reconstructed in the TPC are extrapolated to the MTD, and required to match the hit position as well as the time-of-flight from MTD measurements. Figure 5 show the transverse momentum, p_T, versus the distance between the extrapolation

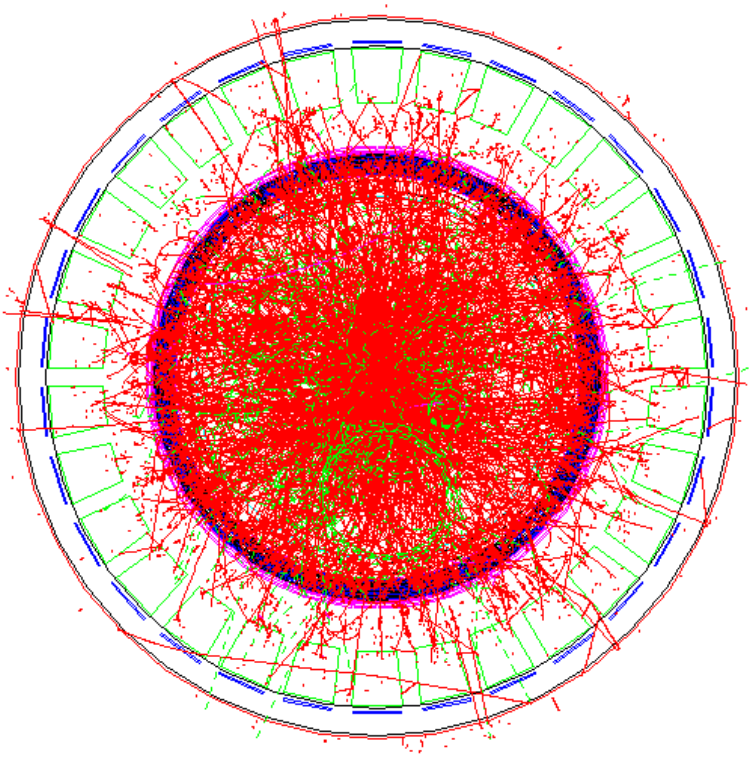

Figure 4. A full HIJING central Au+Au collisions simulated in STAR. The tracks in the TPC are projected in the plane transverse to the beam line.

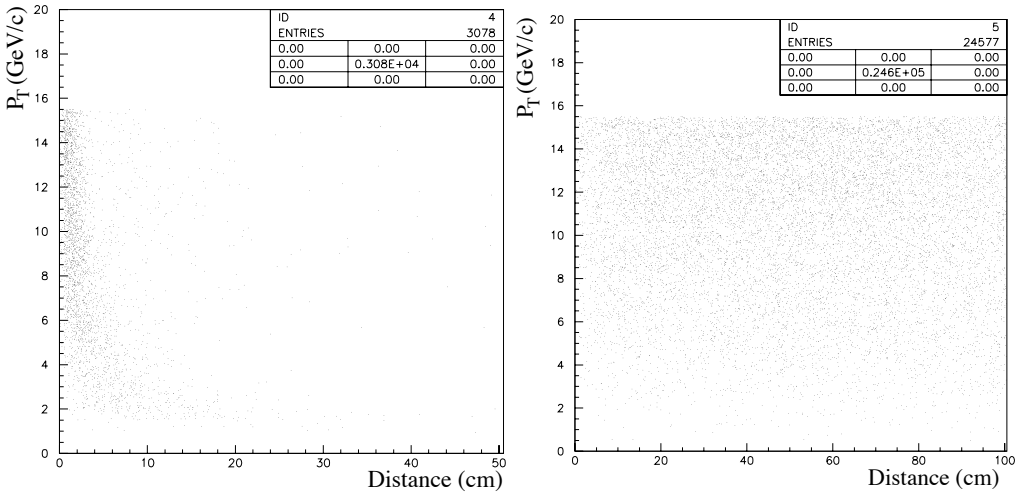

Figure 5. The transverse momentum, p_T, versus the distance between the extrapolation point to the MTD from the TPC tracking and the GEANT hit in the MTD for muon tracks (left frame), and a pion tracks (right frame).

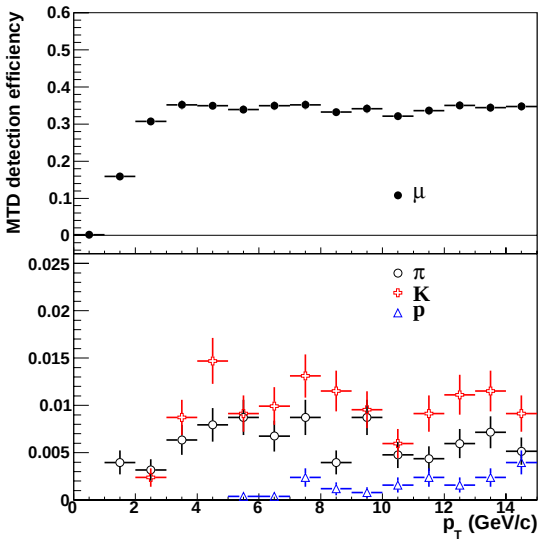

Figure 6. The efficiency for muons (top panel) and misidentification probabilities of pions, kaons, and protons (bottom panel) at $|y| < 0.5$. The inefficiency for muons is mainly due to the acceptance of the MTD (45%).

point to the MTD from the TPC tracking and the GEANT hit in the MTD for muon tracks (left frame) and for pion tracks (right frame). For a pions, the distribution of this distance is very broad due to the strong scattering in the return bar, while for muons, the distribution is much narrower. We require the distance between the MTD hit and the projected point from the track to be less than 4 cm and the timing difference to be less than 400 ps. It should be noted that in this study, a simple helix extrapolation of the track to the MTD was employed. In reality, the magnetic flux return bar has a magnetic field of 1.2 Tesla, and the TPC has a 0.5 Tesla field. Pion and kaon misidentification comes mainly from their decay into muons before the absorption by the return bar. These daughter muons then penetrate the return bars and can reach the MTD. It is also evident from the simulations that protons are reduced by a much larger factor than pions and kaons. During the STAR internal review on the MTD proposal, it was pointed out that the MTD can not cover 56% in full azimuth at $\eta < 0.8$. The MTD trays will sit on top of BEMC boxes outside the magnetic steels. In order to leave enough space for the BEMC operation and maintenance, the MTD acceptance was optimized and the real acceptance was dropped. The detailed discussion can be found at Sect. 8. Shown in Fig. 6 is the combined acceptance and efficiency with the optimized MTD system for primary muons, pions, kaons and protons. It indicates that the MTD can detect muons of $p_T \gtrsim 2$ GeV/c at a level of 36% while less than 1% of the overall hadrons are accepted taking into account the relative yields of pions, kaons, and protons. This illustrates that the MTD detector can reject hadrons effectively. A rejection factor of 50-100 can be obtained based on the simulations shown in Fig. 6 while maintaining an efficient trigger (>80%) for prompt muons. Further hadron rejection can be achieved with

tracking in the TPC, energy loss in the TPC, and hit matching in the TOF. These have been studied in detail with a prototype MTD tray in STAR. The results will be discussed in the next few sections. With the muon efficiency shown above and the measured J/ψ p_T distributions [39, 40], we obtained the J/ψ efficiency versus p_T that is shown in Fig. 7.

4.2. Physics perspectives with full coverage

In this section, we explore the physics potential of a full coverage MTD for STAR at mid-rapidity. The full coverage is the optimized MTD coverage which will not impact the operation and maintenance of the BEMC, as mentioned above. Three physics cases are selected to illustrate the MTD capability for online triggering and improvement of momentum resolution to achieve the physics goals of measuring J/ψ elliptic flow and R_{AA} at high p_T and resolving the ground state Υ from its excited states. In addition, electron-muon correlations can be used to distinguish lepton pair production from heavy quark decays ($c+\bar{c} \rightarrow e+\mu(e)$, $B \rightarrow e(\mu) + c \rightarrow e + \mu(e)$).

Shown in Fig. 7 are the efficiencies for J/ψ at mid-rapidity at RHIC. Both PHENIX and STAR are able to detect the J/ψ at mid-rapidity through $J/\psi \rightarrow e^+e^-$ with electromagnetic calorimeters (EMC) as the trigger device and electron identifier. However, this is limited by the capability to trigger on electrons at low momentum in STAR and relatively lower efficiency times acceptance (ϵ) in PHENIX [41]. STAR can sample the total luminosity delivered at RHIC with a more selective trigger on the interesting events with J/Ψ candidates by EMC towers with a high-energy deposit. However, this reduces the efficiency dramatically at low to intermediate p_T range. The proposed MTD detecting $J/\psi \rightarrow \mu^+\mu^-$ will have much higher trigger rejection power than the STAR EMC and TOF combination and have a larger acceptance than the PHENIX configuration. This results in much larger J/ψ samples than the currently available RHIC experimental setups.

Shown in the top frame of Fig. 8 is the $J/\psi \rightarrow \mu^+\mu^-$ with a signal-to-background ratio of 6:1. The background di-muon pairs are simulated from the inclusive muon yields obtained from studies discussed in subsequent sections. Shown in the bottom frame of Fig. 8 is the invariant mass distribution of di-muons from Upsilon decays simulated in the STAR geometry. Clearly, the different Upsilon states ($\Upsilon(1S)$, $\Upsilon(2S)$, and $\Upsilon(3S)$) can be separated through the di-muon decay channel while Bremsstrahlung energy losses of electrons present a challenge for the separation due to the detector material, including future inner tracker upgrades at STAR. Shown in Fig. 9 are the simulation results of the electron-muon invariant mass distribution from charm pair production and from background. The cross symbols represent the signal. The solid line represents the background, obtained using random combinations between the photonic electron yields measured in d+Au collisions [42] and inclusive muon yields shown in later sections. The signal-to-background ratio for charm pair production is 2:1, if the invariant mass of the electron-muon pair is larger than 3 GeV/c^2 and its p_T is less than 2 GeV/c. The photonic electrons can be paired with other particles in the TPC, which will lead to a factor of 2 rejection. The inclusive muons can be associated with

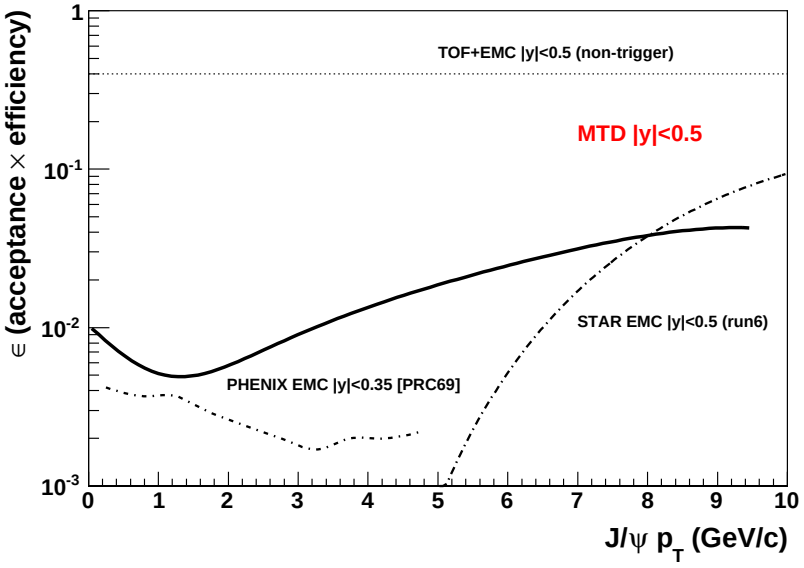

Figure 7. The J/ψ efficiency as a function of p_T. PHENIX [41] and STAR detect $J/\psi \rightarrow e^+e^-$ at mid-rapidity using a combination of several detectors together with electromagnetic calorimeters. The STAR J/ψ efficiency in Run-6 p+p collisions used an EMC high-tower trigger.

the TOF hits, resulting in at least another factor of 2 rejection. If we include these rejection factors, the background will be reduced by a factor of 4, as shown by the dashed line. The signal-to-background ratio for the electron-muon correlation is significantly enhanced.

In the RHIC-II era, when 20 nb^{-1} and 300 pb^{-1} luminosity for Au+Au and p+p collisions is delivered, we expect to get precise J/ψ and Υ measurements in p+p and Au+Au collisions [8]. Figure 10 and 11 show the precision projection of J/ψ R_{AA} and v_2 as a function of p_T. Figure 12 shows the precision projection of Υ R_{AA} as a function of centrality. 20 nb^{-1} Au+Au collisions and 300 pb^{-1} p+p collisions have been used for the projection. These measurements are essential to advance our understanding of the QCD matter created at RHIC. Table 2 shows $\Upsilon \rightarrow \mu^+ + \mu^-$ statistics at the RHIC-II era with the optimized MTD system at STAR. There were doubts on the 200 GeV p+p delivered luminosity. The numbers shown in the table are mainly to show the yields based on given luminosities. If indeed the luminosity is significantly dropped, the Υ counts will be decreased proportionally. On the other hand, the relative yields of Υ(1S), Υ(2S) and Υ(3S) states have been measured at $\bar{p} + p$ collisions at CDF ($\sqrt{s_{\rm NN}}$ = 1.8 TeV) [43] and at p+p, p+d, and p+Cu collisions at fixed target experiment with proton incident energy 800 GeV [44]. The measurements indicate that the relative yield has little dependence on beam energy. At RHIC, the precise measurement on the relative yields of the three states in 500 GeV p+p collisions can provide the reference on the measurements in 200 GeV Au+Au collisions, thus whether the Υ(2S) or Υ(3S) state melts or not in Au+Au collisions can be determined and the temperature of the QGP can be inferred.

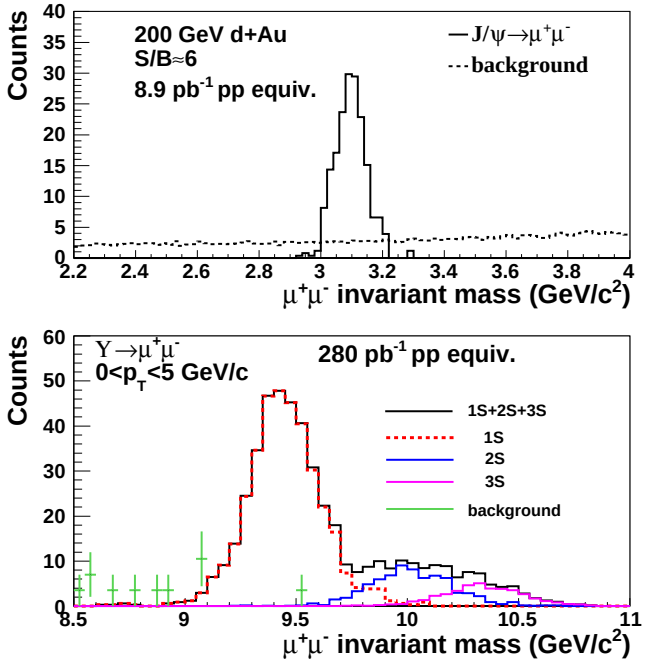

Figure 8. The expected di-muon invariant mass distribution from J/ψ and background in d+Au collisions (top panel); the invariant mass distribution of di-muon decayed from Υ at $0<p_T<5$ GeV/c (bottom panel). The different Υ states can be separated. The equivalent p+p luminosity is also shown in the figure.

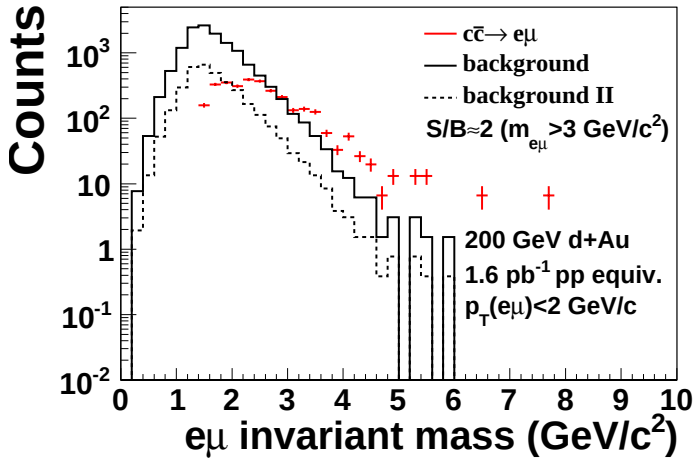

Figure 9. The expected electron-muon correlation from charm pair production and from random background in d+Au collisions. The equivalent p+p luminosity is also shown in the figure.

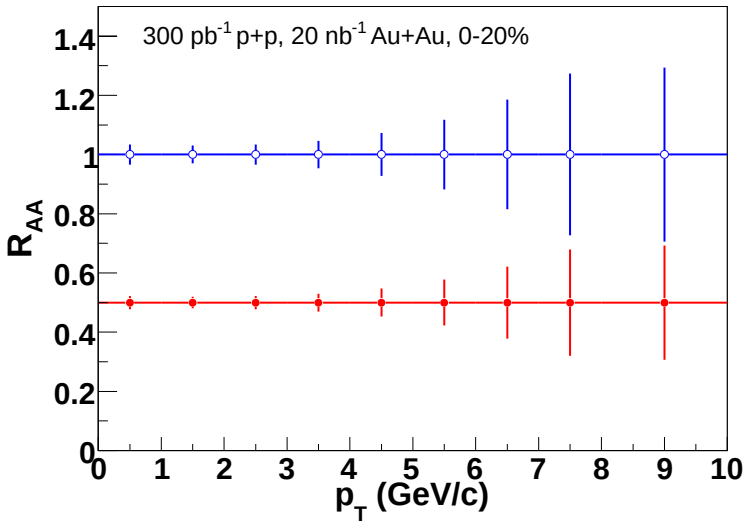

Figure 10. The J/ψ R_{AA} precision projection as a function of p_T with 20 nb^{-1} Au+Au and 300 pb^{-1} p+p collisions at 200 GeV with the optimized MTD system at STAR.

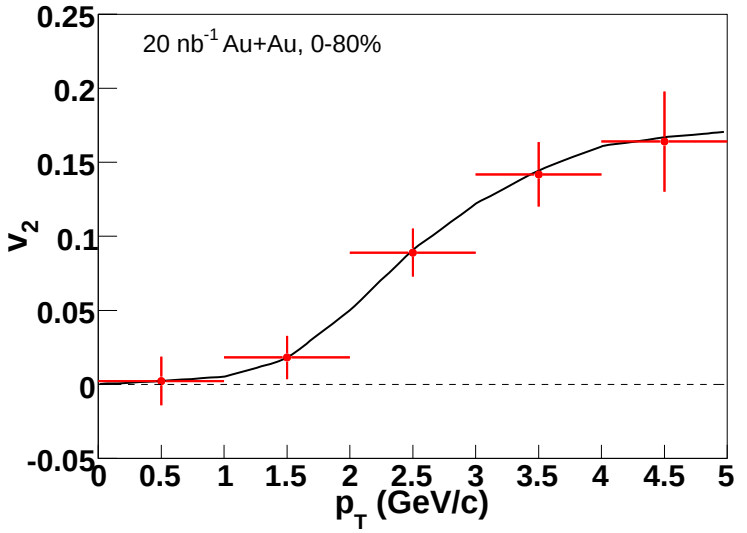

Figure 11. The J/ψ v_2 precision projection as a function of p_T with 20 nb^{-1} Au+Au collisions at 200 GeV with the optimized MTD system at STAR.

5. Trigger Capability

The full muon telescope detector will cover 45% of the TPC acceptance at $|\eta|<0.5$ in order to leave enough space for the BEMC operation and maintenance. If a design similar to the MTD prototype tray is used, there will be 117 LMRPC modules, 1404 read-out strips, and 2808 read-out channels, which are factors of 8-9 less than those in the STAR-TOF system. By using the same electronics design, the full coverage of the MTD system will be very cost effective, and will likely be similar in scope to the smaller RHIC-II upgrades. The trigger

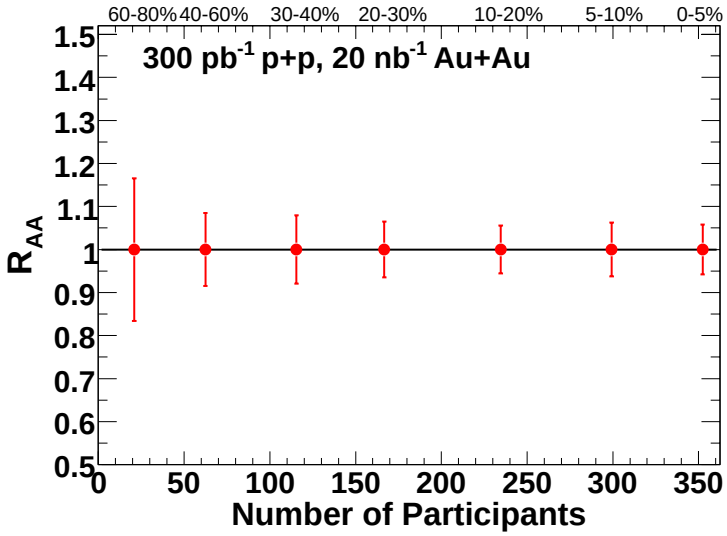

Figure 12. The Υ R_{AA} precision projection as a function of centrality with 20 nb^{-1} Au+Au and 300 pb^{-1} p+p collisions at 200 GeV with the optimized MTD system at STAR.

Table 2. The Υ statistics estimation for different collision systems at RHIC-II era. Deli. Lumi.: delivered luminosity in 12 weeks in 2013. Samp. Lumi.: sampled luminosity in 12 weeks in 2013. According to the efficiency of STAR, we use 70% as the estimation. Min. Lumi.: required sampled luminosity with 10% precision on $\Upsilon(3S)$ state. Min. Lumi.II: required sampled luminosity with 10% precision on $\Upsilon(2S+3S)$ measurement.

collision system	Deli. Lumi.	Samp. Lumi.	Υ counts	Min. Lumi.	Min. Lumi.II
200 GeV p+p	480 pb^{-1}	336 pb^{-1}	930	420 pb^{-1}	150 pb^{-1}
200 GeV p+p	200 pb^{-1}	140 pb^{-1}	390		
500 GeV p+p	1200 pb^{-1}	840 pb^{-1}	6970	140 pb^{-1}	50 pb^{-1}
200 GeV Au+Au	22 nb^{-1}	16 nb^{-1}	1770	10 nb^{-1}	3.8 nb^{-1}

obtains two signals from each backleg (five or three trays). The 12 channels on each end of each of these five or three LMRPCs are combined on the TTRG board to provide an "OR" signal from the earliest discriminator output. Each TTRG board will thus provide an output to the STAR Trigger system, implying a total of 54 cables from the MTD system to trigger QT boards. The details are at Sec. 8.

5.1. Simulation

A full STAR Monte Carlo GEANT simulation of central Au+Au HIJING events has been carried out at the early stage of the R&D to study the trigger capability. The study results in Tab. 3, which shows that timing allows an effective cut for rejecting the backgrounds for the dimuon candidates. Even for central Au+Au collisions, an enhancement of 40 to 200

Table 3. Number of hits per central HIJING Au+Au collision with different cut conditions from MTD. For a dimuon trigger with tight time cuts (-400,+100)ps, we can achieve an enhancement of 40-200. In this simulation, the MTD covers 45% of the TPC acceptance at $|\eta|<0.5$.

Cuts	Nhits/event
No Cut	35
TOF ($\pm$20ns)	0.8
ADC	3.9
TOF& ADC	0.36
TOF (-400,+100)ps	0.12

can be achieved.

5.2. Projection from run7-run8 prototype

Table 4. The trigger rate reduction by requiring a single hit or double hits in the MTD for different collision systems at 200 GeV with full MTD coverage (117 trays in total). L0: single-hit L0 rate output from MTD for a given collision event; L2 with TOF: single-hit rate reduction at L2 trigger with requirement of a TOF hit at the vicinity of the path of a muon candidate (the rate in p+p collisions is measured; the rate in central Au+Au collisions is estimated only, please see Sec. 5.4 in detail); RHIC II Lumi.: RHIC II luminosity in terms of collision rate; dimuon L0 rate: dimuon trigger rate at L0 in Hz at RHIC II; dimuon L2 rate: dimuon trigger rate at L2 in Hz at RHIC II. The numbers in the parentheses are from simulations with a tighter timing cut assuming the electronics can provide $\sim$100 ps resolution. The L0 estimation in run7 and run8 is without timing cut. The L0 estimation in run10 is with timing cut. The details are in the text.

prototype	collision system	L0	L2 w/ TOF	RHIC II (Hz)	dimuon L0 rate (Hz)	dimuon L2 rate (Hz)
run10	min. bias Au+Au	0.044-0.14	–	40 k	80-800	
run7	0-5% Au+Au	0.33(0.13)	$\sim$0.20	50 k	270	$\sim$100 (20)
run7	60-80% Au+Au	0.020	–			
run8	d+Au	0.013	–			
run8	p+p	0.007	0.002	2 M	$\leq$100	$\leq$10

Based on the MTD trigger rate from the prototype tray in Au+Au collisions in year 2007, we estimate that, for the full coverage, the L0 trigger-rate reduction for a single MTD hit will be 0.13 in minimum-bias Au+Au collisions. Therefore the online trigger enhancement for di-muon triggers will reach 59. Table 4 lists the L0 trigger-rate reduction for a single MTD hit with 117 MTD trays in different collision systems, which were estimated from the trigger rates and enhancement factors for the prototype MTD tray in 200 GeV Au+Au collisions in year 2007 and 2010 and d+Au and p+p collisions in year 2008. Table 4 also

indicates the trigger capability in central Au+Au collisions for the di-muon program. The details can be found in Sec. 5.4.

The main comment received from the STAR review committee is related to L0 dimuon rate in Au+Au collisions at RHIC II. If we assume double hits are independent and use run7 prototype performance projection, the rate for L0 di-muon will be 700 Hz; if we assume the Poissonian distribution for the mtd hits, the rate for di-muon will be 300. At STAR, we need to decrease the rate from 300-700 to 100 Hz in order not to impact other physics programs at RHIC II era. The trigger requirement in run7 Au+Au collisions was the signal coincidence of the two scintillator layers between which was the MTD tray. However, the prototype tray in run7 covered a small ϕ angle and is different from what will be used in the full MTD system. This may result in a significant difference on the rate estimation. Also there will be timing readouts at both ends at trigger level which can be used to reject background and have not been taken into account for the rate estimation projected from run7 prototype performance shown in Tab. 4.

5.3. Projection from run10 prototype

In the following, we analyzed the data in Au+Au collisions taken in year 2010 by the new prototype tray, which is close to the one in the full MTD system in terms of the tray acceptance in ϕ and electronics readouts, to illustrate the trigger rejection using the timing cuts. Figure 13 and 14 show the timing difference between the hits from the prototype MTD and the hits from pseudo vertex position detector (tMTD-tVPD) in year 2010 with and without track matching. The broad solid histogram represents the timing difference without track matching, the narrow solid one represents the timing difference with track matching and the dot-dashed curve is the Gaussian fit to the narrow histogram. The timing resolution with track matching is $\sim$500 ps from the Gaussian fit. Table 5 lists the double-hit rejection factor by cutting the timing difference (tMTD-tVPD) within a certain range. The rejection for double hits varies from 50 to 500 depending on the detailed timing difference cuts. Thus the event rate for dimuon trigger in 200 Au+Au collisions at RHIC-II era will vary from 80 to 800 Hz, as shown in Tab. 4. In addition, most of the hits in the narrow distribution are still background. In reality, the background is more shifted toward a later timing, and the muon signal will be more centered toward an earlier timing with a narrower width. Details need to be studied with muon purity selection. Also, we notice that L0 rate without timing cut in year 2010 is higher than what we extrapolate from run7 prototype performance. There might be two reasons behind this: 1) The ϕ acceptance of the prototype tray in run10 is significantly larger and there is a coverage outside the central 52 cm along the ϕ direction outside the backleg steel, as shown in Fig. 15. For the full MTD system, we propose an active area of 89×52 cm^2 for each tray. The coverage outside 52 cm significantly enhances the background rate seen from the simulation and data shown in Fig. 15; 2) The run7 trigger condition was a signal coincidence between two scintillator trays with the prototype MTD tray in-between. In run10, the trigger condition is a valid hit in the MTD. The signal

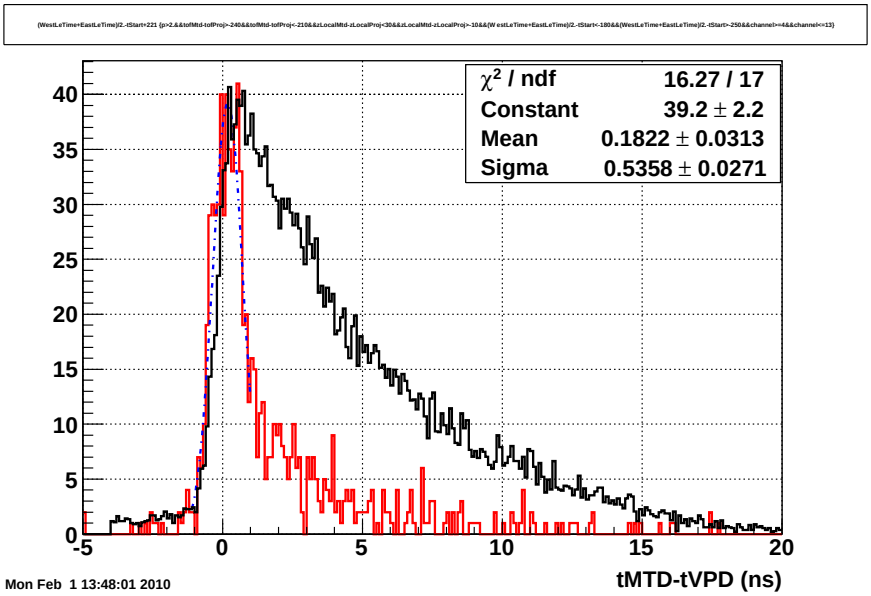

Figure 13. The timing difference between the hits from the prototype MTD and the hits from pseudo vertex position detector (tMTD-tVPD) in year 2010 with and without track matching. The broad solid histogram represents the timing difference without track matching, the narrow solid one represents the timing difference with track matching and the dot-dashed curve is the Gaussian fit to the narrow histogram.

coincidence in run7 might reduce the background generated by a shower track traversing the MTD with a large angle. This might be equivalent to the timing cut as we discussed above in some sense. In the near future, we will adjust the threshold to see the effect on the trigger rate of the prototype tray in year 2010.

Table 5. The double-hit rejection factor by cutting the time difference (tMTD-tVPD) within a certain range in 200 GeV Au+Au collisions. The σ is 500 ps.

selection criterion	double-hit rejection factor
(-2, +2)σ	50
(-2, +1)σ	116
(-2, 0)σ	509

5.4. Additional rejection with TOF hits

In p+p collisions it was found that when there was a coincidence with the hit in the TOF detector in the same TPC sector, the trigger rate was reduced by a factor of 3. From the extrapolation of a valid MTD hit and the time difference measured between the VPDs on the east and west sides of the interaction point, the expected hit position in the TOF system was

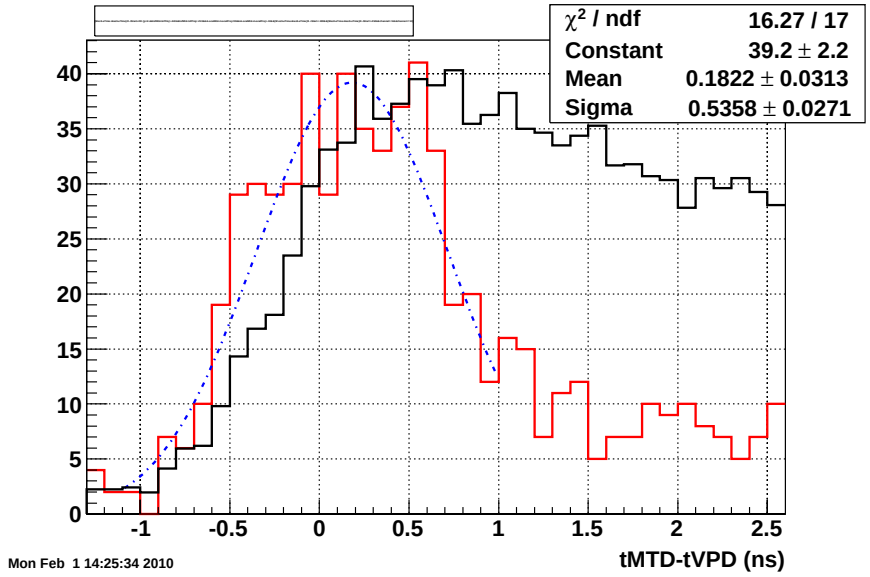

Figure 14. The timing difference between the hits from the prototype MTD and the hits from pseudo vertex position detector (tMTD-tVPD) in year 2010 with and without track matching. This is a zoom-in version of Fig. 13.

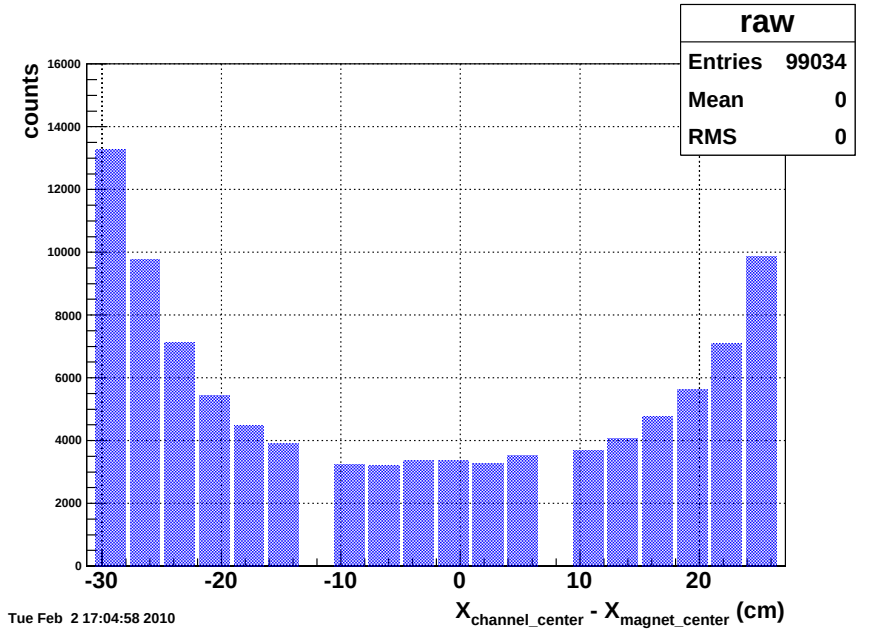

Figure 15. The MTD raw hits distribution along the ϕ direction in 200 GeV Au+Au collisions in year 2010. There are three LMRPC modules, 18 strips in total. The strip size is 87×2.5 cm^2.

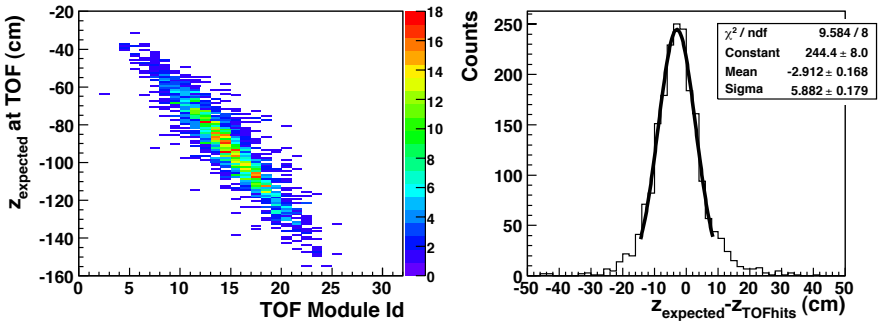

Figure 16. The expected Z position at the TOF system versus the module ID with a valid hit in 200 GeV p+p collisions in year 2008. The modules in the TOF system are sequentially positioned along the z direction (left panel); the distributions of the difference between the expected position and the measured position along the z direction from the TOF system (right panel). The expected position ($z_{expected}$) is obtained from the extrapolation of a valid MTD hit and the time difference measured between the VPDs on the east and west side of the interaction point.

obtained. From the TOF system, the module ID with a valid hit leads to another position measurement since the modules in the TOF system are sequentially positioned along the z direction. Shown in Fig. 16 (left panel) is the extrapolated z position versus measured module ID with a valid hit in the TOF system in 200 GeV p+p collisions. Strong correlations were observed. The difference of these two z values are shown in the right panel of Fig. 16. A single Gaussian was used to fit the distribution and the sigma was found to be ∼6 cm. Combining the information in the MTD and TOF system, we can obtain more than an order of magnitude rejection dramatically increasing the efficiency for dimuon triggers in central Au+Au collisions at 200 GeV, as shown in Tab. 4.

6. Performance of a Prototype MTD

We utilize LMRPCs for the detector design. Each prototype LMRPC module consists of two stacks of resistive glass plates resulting in a combined total of ten uniform gas gaps with gap widths of 250 μm. High voltage is applied to electrodes on the outer surfaces of the outer glass plates of each stack. A charged particle traversing a module generates avalanches in the gas gaps which are read out by six copper pickup strips with strip dimensions of 870×25 mm^2. Figure 17 shows the side and top view of an LMRPC module prototype. The MRPC modules were operated at 12.6 kV with a mixture of 95% $C_2H_2F_4$ and 5% iso-butane at 1 atmosphere. In the high voltage range between 12.5 and 13.0 kV, the efficiency is above 95% and timing resolution is about 60-70 ps in the cosmic ray and beam tests. The spatial resolution of the LMRPC along the long strip is about 0.6-1 cm in the same tests. This satisfies the needs for a large-area muon detector. The details of the LMRPC construction and its performance in the cosmic ray and beam tests can be found in this paper [45] and in

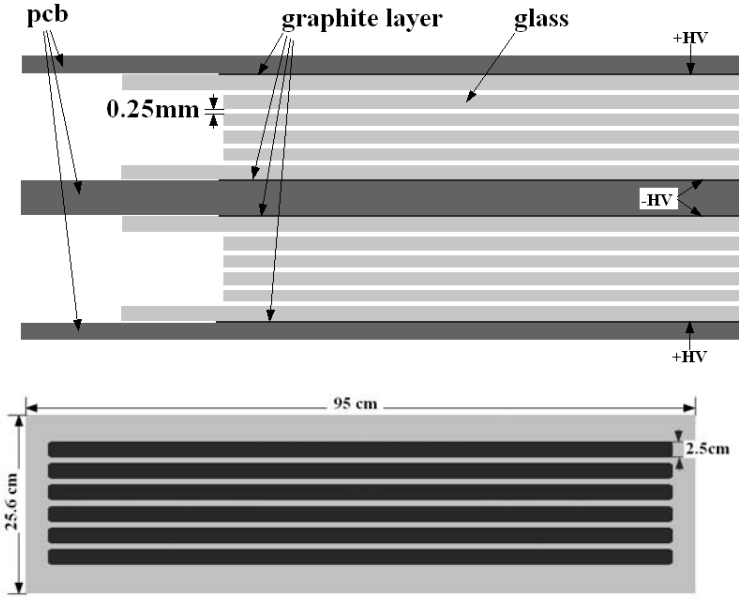

Figure 17. Side view and top view of an LMRPC module prototype.

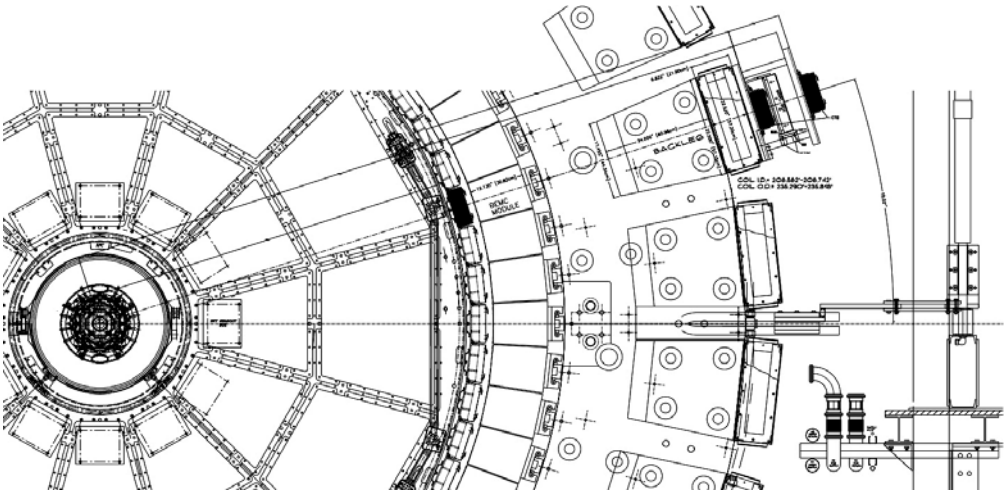

Figure 18. Position of the MTD prototype at STAR. Three backlegs and their BEMC PMT boxes are shown on the right in this plot, while the TPC is on the left. The MTD prototype is on top of one of the BEMC PMT boxes at a radial distance of 400 cm from the interaction point.

Sect. 7.

A prototype of the MTD was installed and covered $\pi/60$ in azimuth and $-0.25<\eta<0.25$ in pseudorapidity at a radius of $\sim$400 cm during the 2007 run in 200 GeV Au+Au collisions. During the 2008 run in 200 GeV d+Au and p+p collisions, the prototype was re-located and covered $-0.5<\eta<0$ in pseudorapidity at the same radius. It contained two LMRPC modules. The prototype was placed outside of the return bars which serve as hadron absorbers, each of

Table 6. Trigger rates, sampled luminosities, recorded events and matched hits with TPC tracks at $p_T > 1.5$ GeV/c in Au+Au, d+Au and p+p collisions in year 2007 and 2008 with the prototype MTD.

beam species	interaction rate (Hz)	trigger rate (Hz)	sampled luminosity	recorded events (M)	matched hits
Au+Au	20 k	0.5–2	270 μb^{-1}	0.31	7 k
d+Au	100 k	0.5–2	29 nb^{-1}	1.6	78 k
p+p	300 k	0.5–2	404 nb^{-1}	0.56	8 k

which amounts to 5 interaction lengths. A mechanical drawing of the location and geometry of the MTD in STAR is shown in Fig. 18. The analog signals [46] were sent to trigger digitizer boards specially developed for use in the STAR trigger system [47] for signal amplitude and timing information read-out. Each digitizer board consists of an 8-bit analog-to-digital converter (ADC). In addition, discriminator outputs from the digitizer boards with thresholds set to 30 mV were routed to a time-to-analog converter (TAC), which was gated by the RHIC accelerator clock. The TAC signals were sent to a different channel of the digitizer board. Both ADC and TAC values were routed through the trigger distribution and processing system for an initial Level-0 ("L0") trigger decision [47]. The L0 trigger is generated in less than 1.5 μs from all the fast detector information available for triggering and is used to start the digitization process on slower detector systems (e.g. TPC). We have not required time difference or any other matching algorithms for a trigger decision as discussed in the simulation. A valid hit was required to have a non-zero and non-overflow ADC and TAC value within the 8-bit digitizer board range. The prototype successfully triggered the data acquisition system by requiring a valid hit in at least one strip of the LMRPCs. Table 6 lists the trigger rates, sampled luminosities, and recorded events with the prototype MTD in Au+Au, d+Au, and p+p collisions in years 2007 and 2008. For the run in 2009, we installed a different prototype tray, which was equipped with the same electronics as is used in the STAR-TOF system [7] to further improve the timing resolution of the MTD. The TOF electronics have a time bin width (25 ps) that is small compared to the detector resolution, and the degrading effects of the long cables are removed as the digitization will be done on-board the detector. The addition of the TOF-based electronics is expected to allow a significant improvement to the MTD's timing measurement in the off-line analysis.

Shown in Fig. 19 is the azimuthal angle distribution of particles from the TPC extrapolated to a radius of 400 cm in triggered d+Au collisions as a function of the transverse momentum p_T. In the track-by-track extrapolation, a realistic magnetic field map was generated and used. The magnetic field in the return bars is 1.2 Tesla, when the field in the TPC is 0.5 Tesla. The effect of energy loss was taken into account when muons traversed the steel. Alternatively, we used a GEANT simulation with the STAR geometry, implemented the realistic magnetic field map, and generated a look-up table of position and momentum from the last tracking point of the TPC to the MTD detector location. The projection was then done with this look-up table. The results from these two methods are consistent and

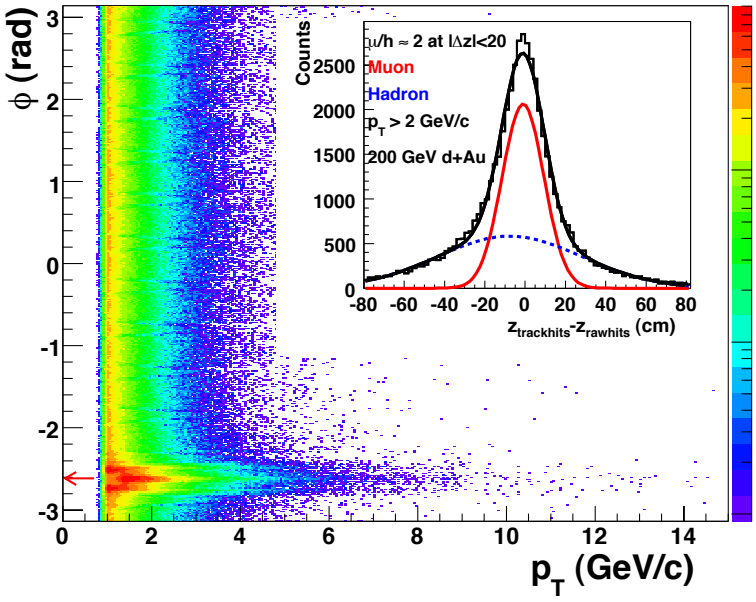

Figure 19. Azimuthal angle distribution of particles, versus p_T in d+Au collisions, extrapolated from the TPC to a radius of 400 cm. The arrow denotes the azimuthal location of the prototype MTD tray. The insert shows ΔZ distribution. $z_{\rm trackhits}$ is derived from extrapolation of the tracks of the TPC to the MTD location. $z_{\rm rawhits}$ is measured by the time difference from two-end readout of the hit strip along the long strip of the LMRPC.

the track-by-track extrapolation was used in this proposal. The peak in Fig. 19 shows an enhancement of particle yield at the angle where the MTD is positioned. This shows that offline tracking of particles from the TPC was able to match hits from the LMRPC. The tracks of the TPC were extrapolated to the MTD location, resulting in position information from tracking. The time difference from two-end readout of the hit strip provides a position measurement along the long strip of the LMRPC. The MTD is placed behind the backleg steel of the magnet, thus multiple hits are not an issue. The difference of these two position values in the z direction (Δz) is shown in the insert of Fig. 19, where the z direction is the beam direction. A double Gaussian function was used to fit the distribution. The σ of the narrow Gaussian was found to be ∼10 cm by selecting tracks of p_T>2 GeV/c, while the other Gaussian is significantly broader. The ratio of the particle yields in the narrow Gaussian to those in the broad Gaussian, within our match window of $|\Delta z|$<20 cm, (the narrow-to-broad ratio) is ∼2. Table 6 lists the total matched hits within the match window $|\Delta z|$<20 cm at p_T> 1.5 GeV/c in Au+Au, d+Au, and p+p collisions with the prototype MTD. From the GEANT simulation, muons of p_T∼2.5 GeV/c generated at the center of the TPC result in a Gaussian distribution with a sigma of 9 cm in the z direction in the MTD barrel, after traversing the detector material from the TPC center to the MTD. The simulation also indicates that pions will result in a much broader distribution due to the strong interaction.

6.1. Muon identification capability and hadron rejection

At p_T>2 GeV/c, the dE/dx of a muon track is ∼3-4% higher than that of a pion track [48]. The resolution of the dE/dx in the TPC is ∼8% [30], therefore, a half sigma difference in dE/dx is expected between a muon and a pion track. About a two-sigma difference is expected between a muon and a kaon track. The energy loss due to multiple scattering in the return bar will cause an energy loss of ∼1.2 GeV for muons with 2<p_T<10 GeV/c, while the velocity change is negligible. For hadrons, the strong interaction will lead to a hadronic shower. This results in a significant energy loss and a change of velocity, and therefore a later arrival at the MTD. By selecting high velocity and large dE/dx particles, the hadron background was observed to be significantly reduced and the narrow-to-broad ratio was found significantly enhanced. This is consistent with the expectation that the narrow Gaussian is dominated by muons and the broad Gaussian is dominated by hadrons. Within the match window $|\Delta z|$<20 cm, muon purity can be achieved to greater than 80% through the combined information of track matching, dE/dx, and velocity.

The average LMRPC timing resolution for the two modules used in this analysis was measured to be ∼300 ps in Au+Au collisions. The "start" time was provided by two identical vertex position detectors (VPDs), each 5.4 meter away from the nominal collision point along the beam line [49]. After subtracting the start timing resolution (∼160 ps) and detector material effect contribution (∼100 ps at p_T=2.5 GeV/c), the timing resolution ($200 - 300$ ps) from the MTD was found to be worse than from cosmic ray and beam tests. This is understood by the fact that the trigger read-out electronics was not designed for a precise time measurement. With the proposed full-scale detector, we will use TOF electronics. TOF electronics have a timing resolution of 25 ps. It has proven to be a low-cost, reliable system for recording timing information, reading it out, and sending it to the STAR DAQ. The electronics boards used for the TOF can be used for the MTD without any significant design changes.

To further assess the pion contamination, we identify the pion tracks which come from the K^0_S weak decay through the hadronic decay channel $K^0_S \rightarrow \pi^+\pi^-$ to measure the fraction of muon candidates from pion decays. $K^0_S \rightarrow \pi^+\pi^-$ was reconstructed through V0 decay topology. Shown in Fig. 20 (top panel) is the raw K^0_S mass distribution from pion pairs reconstructed in other azimuthal angles away from the MTD while in the bottom panel is the raw K^0_S yield with at least one of the daughter pions associated with an MTD hit. The dot-dashed line depicts the K^0_S yields from a projection assuming that the particles associated with MTD hits are all from pion decays. We found the secondary muons from pion decay contributed 30-40% to the total muon candidates. The remaining background contaminating the prompt muon candidates was due to secondary muons from kaon decay. This can be investigated using the difference of the TPC track dE/dx for kaons and muons. By cutting on a high dE/dx value of $n\sigma_\pi$>0, where $n\sigma_\pi$ is the measured dE/dx normalized by the value expected for pions dE/dx [31], we reject part of the kaon secondary decay products. Furthermore, from p+p MTD-triggered events taken in year 2008, we found that

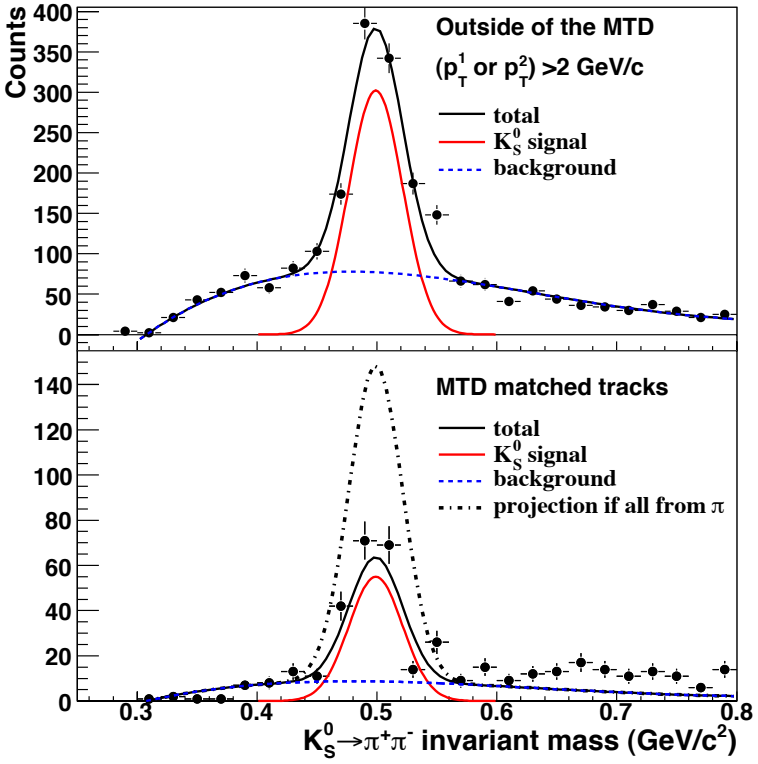

Figure 20. Reconstructed K_S^0 which are not associated with MTD triggered particles (top panel); reconstructed K_S^0 with at least one of the daughter pions associated with the MTD triggered particle. The dot-dashed line depicts the K_S^0 yields from a projection assuming that the particles associated with MTD hits are all from pion decays (bottom panel).

the inclusive muon yields can be decreased by a factor of 2 by requiring a coincidence with a valid hit in the TOF system in the same TPC sector.

Table 7. The fraction of TPC tracks which match with a non-zero EMC energy ($>$ MIP) from non-MTD sectors (A), and the fraction of TPC tracks which match with a non-zero EMC tower energy ($>$ MIP) and a MTD hit (B). A non-zero EMC energy is defined to be > 0.75 GeV above pedestal.

p_T (GeV/c)	EMC & non-MTD (A)	EMC & MTD (B)
1.5–2	$(2.21 \pm 0.03)\%$	$(0.18 \pm 0.02)\%$
2–3	$(3.67 \pm 0.07)\%$	$(0.30 \pm 0.04)\%$
3–4	$(5.89 \pm 0.22)\%$	$(0.34 \pm 0.10)\%$
4–6	$(7.92 \pm 0.50)\%$	$(0.65 \pm 0.24)\%$

We not only use several detectors (TPC, TOF and MTD) to improve the muon identification, but also use additional detectors to check the effectiveness of hadron rejection. One of the methods is to use hadronic showers in the BEMC to study the fraction of inclusive

muon candidates from hadron showers starting at the EMC and penetrating the absorbers. Only a few percent of hadrons produce showers and deposit energy above the minimum ionization energy (MIP) in the BEMC. Table 7 shows the fraction of hadrons with energy deposited in the BEMC greater than 0.75 GeV with and without an associated MTD hit. There is a factor of ≥ 10 reduction of hadronic showers in the BEMC, when we require muon candidacy in the MTD. Since the electron yield is about 0.1% of the inclusive hadron yield in year 2008 in 200 GeV p+p collisions at STAR [42], it is reasonable to assume that all of the BEMC showers with a TPC track are hadrons when an MTD hit is not associated. This means that the contribution from hadrons was reduced from $\simeq 100\%$ to $\leq 10\%$ while that from muons (both prompt and from hadron decays) increased to $\geq 90\%$ of the remaining sample. By comparing the difference between the BEMC showers with and without the MTD hit requirement, we conclude that particles which arrive at the BEMC when there is a valid MTD hit in coincidence are indeed dominated by muons. However, the muons are primarily from pion and kaon decays in the first 2 meters of the STAR detector.

Since the prompt muons are predominantly from charm semi-leptonic decays, we compare our muon yields to non-photonic electron yields in the same p_T bin to assess the muon contamination from pion and kaon decays. The raw yields of muons were obtained from Gaussian fits to the distributions of Δz. The narrow component is attributed to the muons. The systematic uncertainty on the muon raw yields from different fit ranges and parameter constraints is about 20%. The acceptance and efficiency were studied in simulations and used to correct the yields. The ratio of the raw yields $d^2N/(2\pi p_T dp_T dy)$ of inclusive muons, $(\mu^+ + \mu^-)/2$, to the non-photonic electron yields in 200 GeV d+Au collisions at mid-rapidity are shown in Fig. 21 for different muon selection criteria. Also shown in Fig. 21 is the pion-related contribution to the inclusive muon yield as a function of p_T, evaluated by reconstructing K^0_S with at least one of the daughters associated with an MTD hit, as described above in detail. The non-photonic electron invariant yields are from STAR publications [50]. Compared to the non-photonic electron yields, the primary muons contributed 6-10% to the inclusive muons if only MTD hit association was applied. Table 8 lists the primary muon selection efficiency and the ratio of primary to secondary muons from pion and kaon decays (S/B) under different selection criteria on the dE/dx. By selecting a high dE/dx value of $n\sigma_\pi$>1, the S/B ratio increased by a factor of 3, as shown in Table 8.

Table 8. The signal-to-background ratio and primary muon selection efficiency under different conditions in 200 GeV d+Au collisions. The S/B ratio is p_T dependent.

selection criterion	primary muon efficiency	the S/B ratio
without cut	100%	1/15–1/9
$n\sigma_\pi$>0	61%	1/10–1/6
$n\sigma_\pi$>1	26%	1/6–1/3

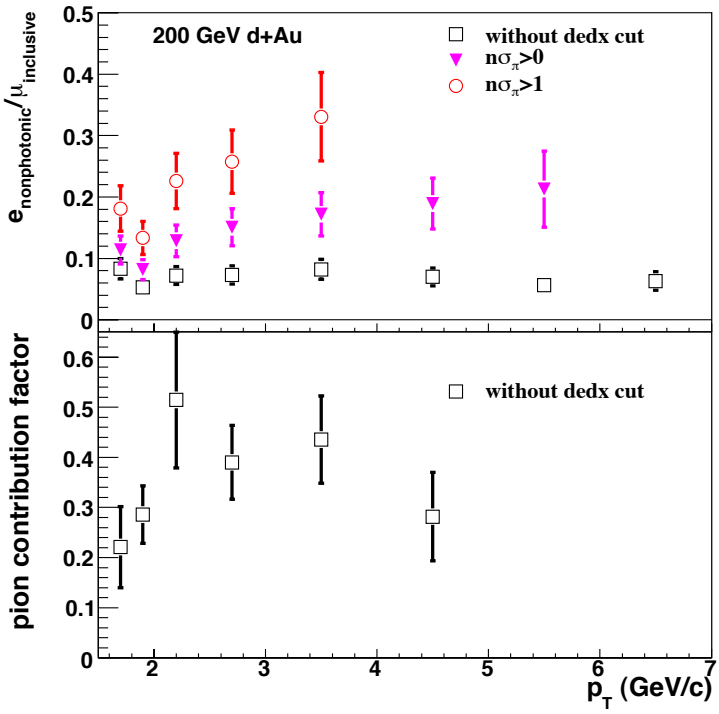

Figure 21. Estimation as a function of p_T of the fraction of detected muons which are prompt by comparison of the total inclusive muon yield to the measured yield of non-photonic electrons (electrons not resulting from photon conversions, hadron decays, or Dalitz decays). The estimate is made with and without cuts on the ionization energy loss (relative to that expected for a pion) in the TPC for the track projected to the position of the MTD. Since the dE/dx for a muon in the relevant momentum range is higher than that for a pion, increasing the cut on $n\sigma_\pi$ results in a higher fraction of prompt muons (top panel); the contribution from pion decays to the measured inclusive muon signal as a function of p_T, determined by measuring the MTD response when a pion from a K^0_S decay enters its acceptance (bottom panel).

7. Test Beam and Cosmic Ray Test Results

7.1. Cosmic Ray test

The prototype module was tested with cosmic rays using the set-up shown in Fig. 22. Three scintillators were used to define a triggered area of 20×5 cm^2 along the read-out strips. This trigger area fully covered one LMRPC strip in width (the "strip under investigation") and half each of the two neighboring strips. Two of these scintillators were read out at both ends with four fast Photomultiplier Tubes (PMTs) which provided the event reference time (T0). A STAR-TOF MRPC module [7] also covered the triggered area with six read-out pads, which divided the triggered area into six segments with area of 3×6 cm^2. The LMRPC signals were read out from both ends via the front-end electronics based on MAXIM 3760 chips [46]. These electronics provided both amplification and discrimination. For additional

details on the cosmic tests, see Ref. [45].

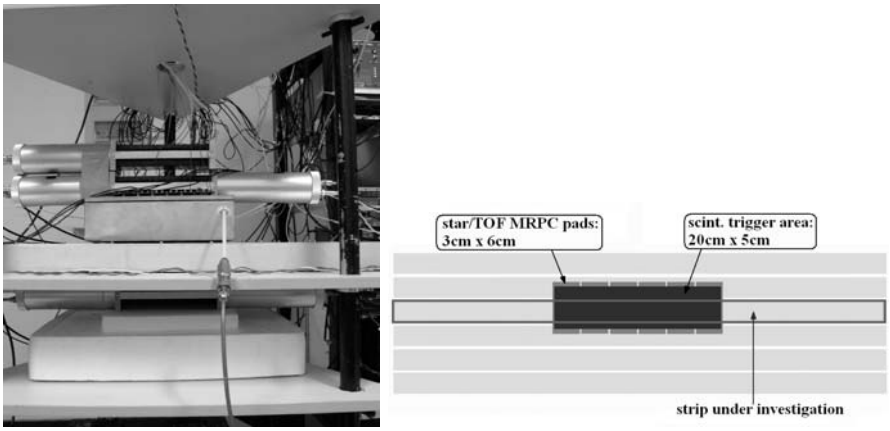

Figure 22. The set-up used for the cosmic ray tests.

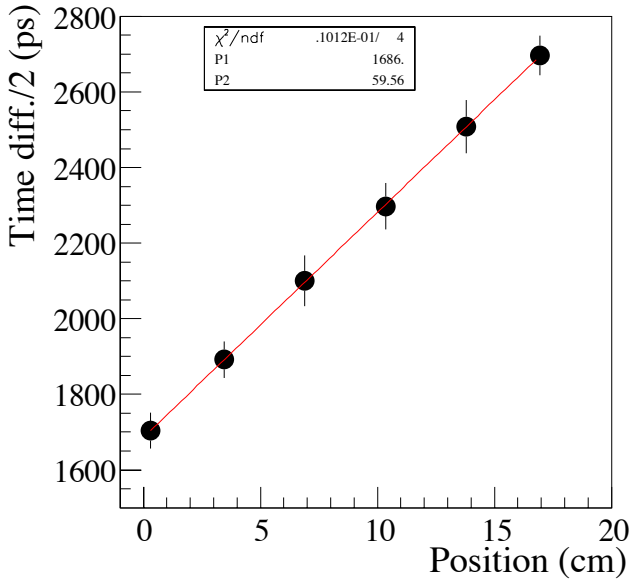

Figure 23. Time difference from the two-ends of the LMRPC strip vs the hit position.

The six pads of the STAR-TOF MRPC gave a rough position along the readout strips. Figure 23 shows the relationship between one-half of the time difference measured from the two ends of the investigated strip and the relative hit position. The slope of the linear fit indicates the reciprocal of the signal propagation velocity along the strip, which is observed to be 59.6 ps/cm. Figure 24 shows the relationship between the charge of the signals taken from the two ends (left and right) of the read-out strip under investigation. The left frame of this figure shows this relationship when the triggered area was placed in the middle of an LMRPC strip, while the right frame shows this relationship when the triggered area is at an extreme end of the read-out strip. Even in the latter case when the signal transmitting

distances to left and right are quite different, a linearly correlation can still be observed. This indicates that the attenuation of pulse area along the strip can be neglected.

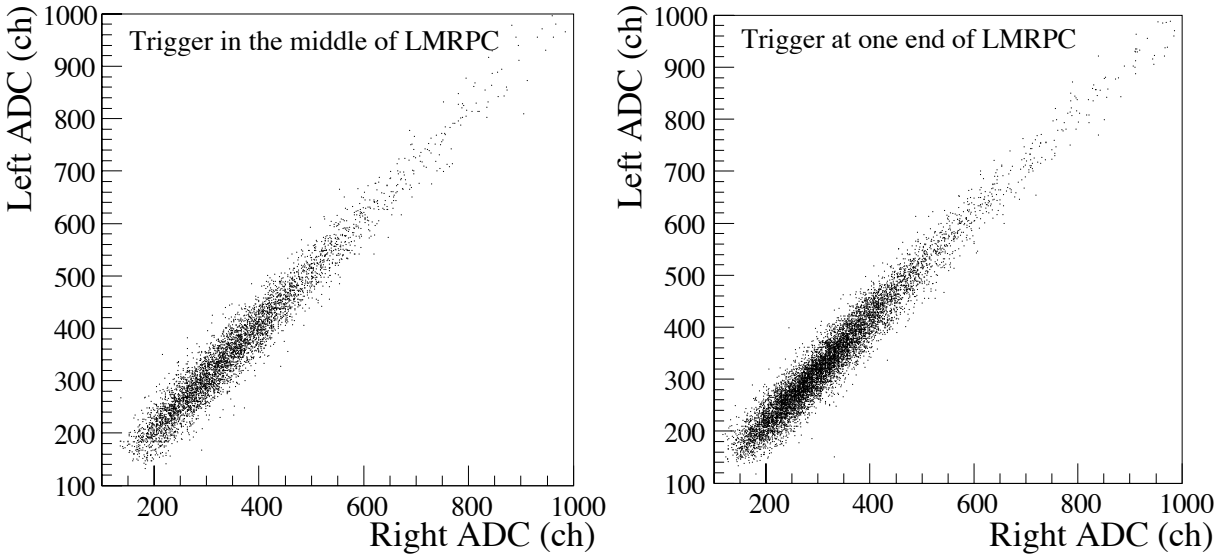

Figure 24. The charge sharing and attenuation between the two ends of an LMRPC strip for hits at the middle of an LMRPC strip (left frame) and at one end of an LMRPC strip (right frame).

The mean time, $T_{mean}=(T_{left}+T_{right})/2$, formed from the time from the two ends of one strip eliminates the time smearing caused by the position of the hit along the strip. The signals from two ends had been found to be similar in area. Thus, the slewing correction was made between the arithmetical mean of time and pulse area (mT-mA correction). A sixth-order polynomial was fit to these curves to obtain the slewing correction function. The reference time resolution was 98 ps. The distributions of mean time with respect to the reference time after the mT-mA correction are shown in Fig. 25. Following the subtraction of the reference time resolution in quadrature, the time resolution of the LMRPC itself was observed to be 60 ps when triggered in the middle of the module, and 74 ps when triggered at one end.

7.2. Beam Test at FermiLab

A beam test experiment (T963) was carried out at the MTEST facility at Fermi National Accelerator Laboratory in May 2007. The beam consisted primarily of 32 GeV muons, pions, and protons. The set-up of the beam test is shown in Fig. 26. Two LMRPC modules were tested. One was made at Tsinghua University (MRPC1, upstream) and the other was made at the University of Science and Technology of China (MRPC2, downstream). These were placed on a movable platform. TOF1, TOF2, and TOF3 are three layers of scintillators. The coincidence of TOF1 and TOF2 was used as the event trigger and the common start signal for the TDCs. TOF3 provided the reference time for the LMRPCs. Nine layers of

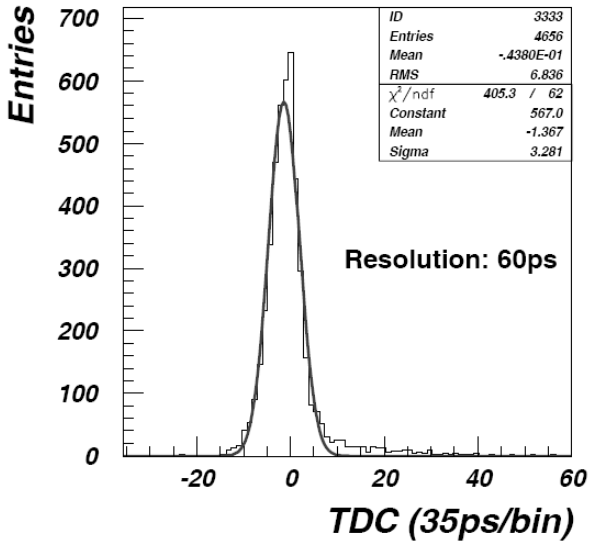

Figure 25. Time difference from the two ends of the LMRPC strip versus the hit position.

Multi-wire Proportional Chambers (MWPCs) and three layers of Gas Electron Multiplier (GEM) chambers provided the beam particle position at the LMRPCs. Two Cherenkov detectors (C1 and C2) were used for beam particle identification.

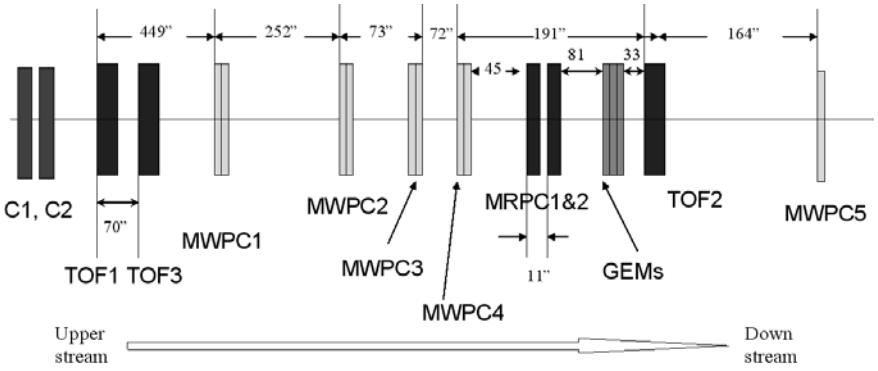

Figure 26. Layout of the T963 test beam setup at Fermilab Test Beam Facility.

Figure 27 shows the detection efficiency plateau of the USTC module. The electric field E in the gas gaps is equal to the applied HV values (the absolute sum of the positive and negative values) divided by the total thickness of all of the gas gaps (250 $\mu m \times 5$) in one stack. Over a wide range of working electric field values (90-104 kV/cm), the detection efficiency is greater than 98%. After the slewing correction and the subtraction in quadrature of the reference time resolution, the LMRPC time resolution is plotted versus the electric field and shown in Fig. 28. The time resolution is less than 70 ps for electric fields between 100-105 kV/cm.

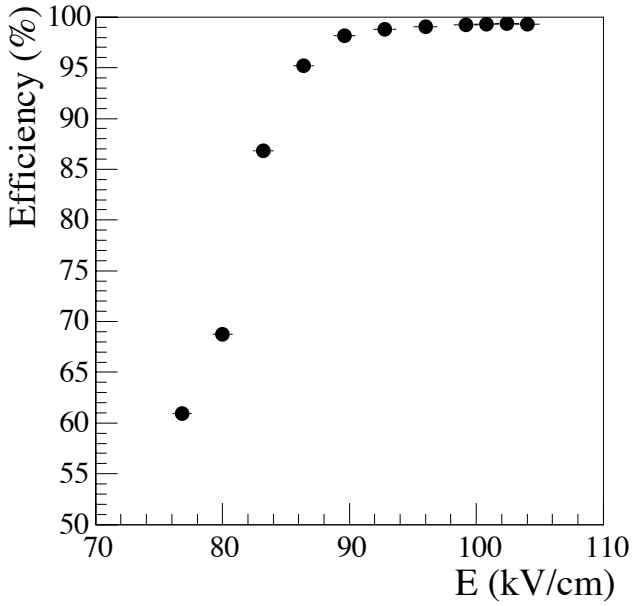

Figure 27. LMRPC efficiency as a function of the electric field by the applied HV.

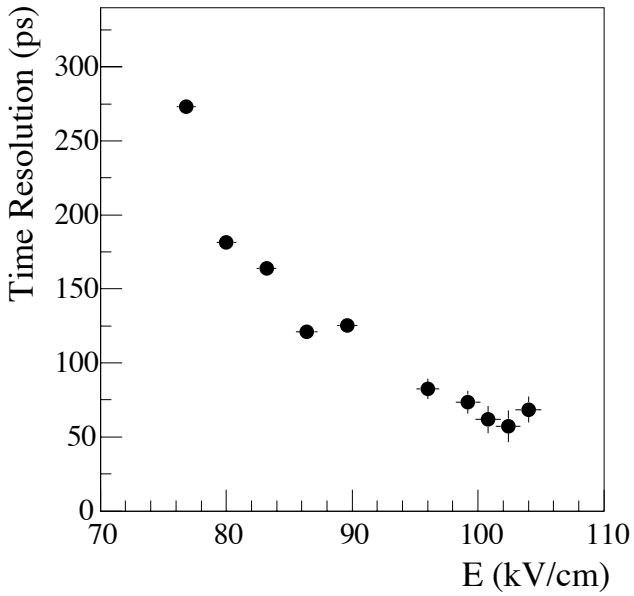

Figure 28. LMRPC timing resolution as function of the electric field.

The correlation between the difference of the times measured from the two ends of one LMRPC strip and the incident particle position is shown in Fig. 29. The strong correlation that is observed confirms that the time information can be used to calculate the position of the hit along the strip. The slope of the linear fit indicates a signal propagation speed of ∼60 ps/cm, which is consistent with that obtained from the cosmic ray tests. Shown in the left frame of Fig. 30 is a scatter plot of the beam particle position as measured by the GEM

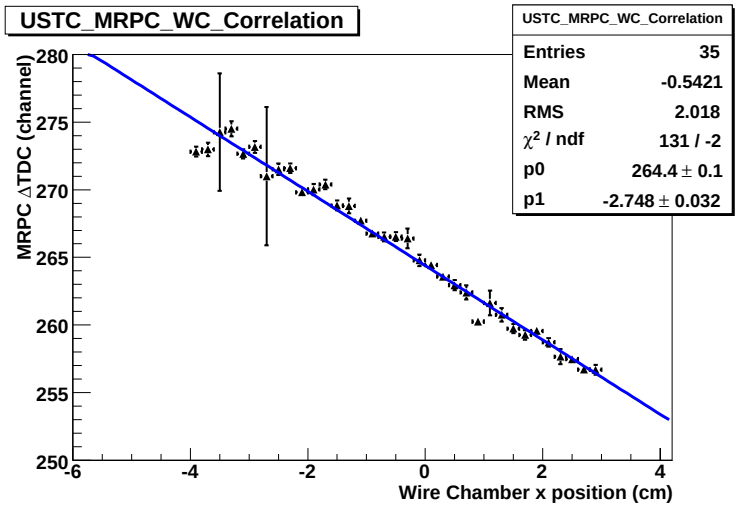

Figure 29. The time difference from the two ends of an LMRPC versus the incident particle position determined by the wire chamber.

detectors versus the LMRPC hit position obtained with the difference of the times at the two ends of one strip. The variance of this correlation is shown in the rght frame of Fig. 30. This variance is observed to be 0.6-1.0 cm, and is assumed to result purely from the LMRPC spatial resolution since the spatial resolution of the GEM is $\sim$70 μm.

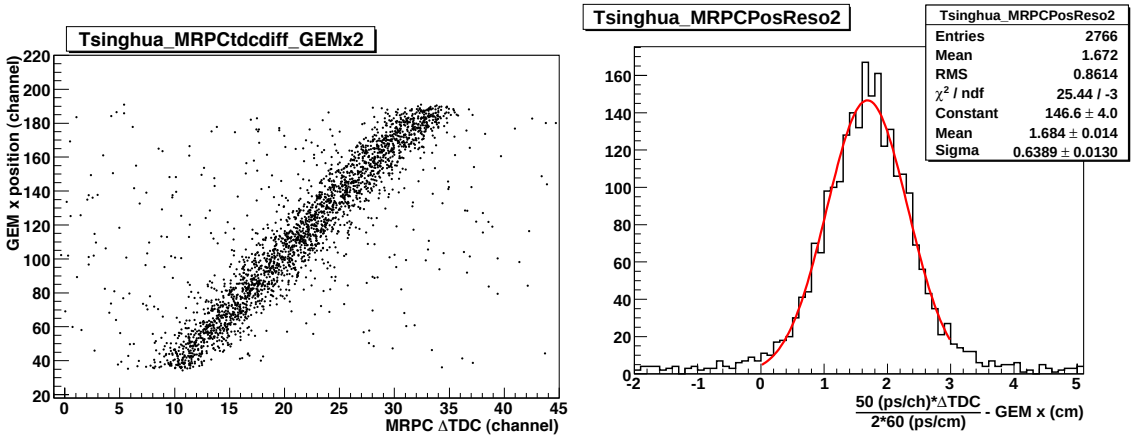

Figure 30. On the left is the hit position from the GEM chambers versus the hit position from the LMRPC left-right time difference, and on the right is the spatial resolution of the LMRPC along a strip.

8. Construction

8.1. Detector Configuration

To meet the physics objectives outlined in the previous section, the MTD system must measure time intervals using the information on the track momenta and positions determined

by a separate system (the TPC) and projected through the return yokes to the MTD. The aspects of the detector system needed to successfully operate in STAR and achieve the required level of hadron rejection are described in this section. This is followed by detailed descriptions of the design of the MRPC detectors (Sect. 8.2), the mechanical components (Sect. 8.3), the gas system, and the electronics (Sect. 8.4).

The MTD detectors will be placed at a radius of 400 cm from the interaction point. They will be located on top of the BEMC boxes outside the steel backlegs as shown in Fig. 31. The long strips will be parallel to the beam direction. In order to leave enough space for the BEMC operation and maintenance, the total number of MTD trays will be 117. There are 3 backlegs at 3 o'clock and 9 o'clock direction outside which we can not put any MTD tray. For the bottom 9 backlegs, there will be 3 trays in each backleg; for the other 18 backlegs, there will be 5 trays in each backleg. In total, there will be 117 trays. In each tray, there will be one LMRPC module. The active region of each LMRPC will be 89 cm in length (along the beam direction), and 52 cm in width (azimuthally). Each module has 12 strips, and each strip is read out from both ends.

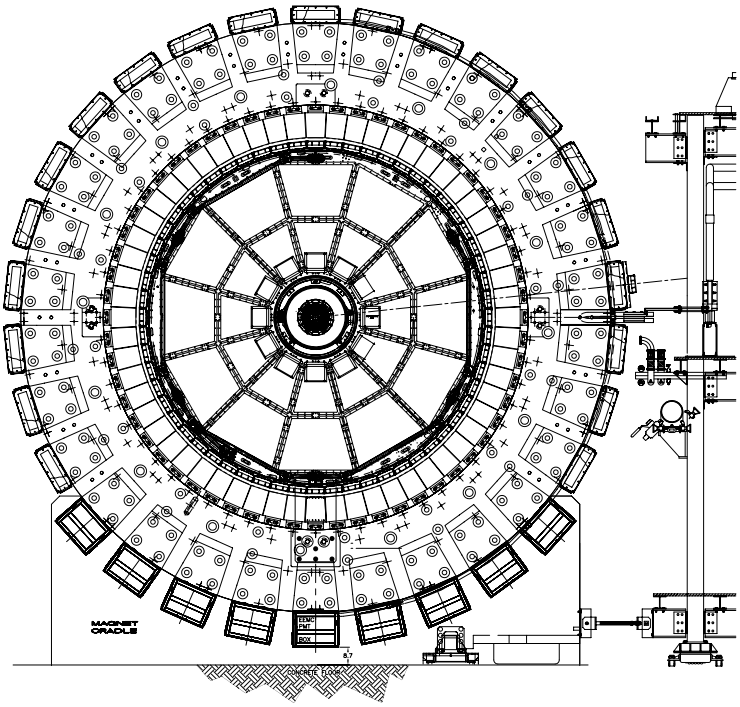

Figure 31. A beam's eye view of STAR. The outermost boxes in radius are the BEMC PMT boxes which are mounted directly to the magnet return yolks. The MTD system will attach to these PMT HV boxes. There are 3 backlegs at 3 o'clock and 9 o'clock direction outside which we can not put any MTD tray. For the bottom 9 backlegs, there will be 3 trays in each backleg; for the other 18 backlegs, there will be 5 trays in each backleg.

For the system to meet the physics objectives, the critical requirements are those on the total time interval resolution, and the spatial resolution from the time differences between

the two ends of a strip. The complete list of system constraints and requirements is as follows:

- The total time interval resolution after all corrections must be comparable to that of the TOF system (100 ps). This will provide a position resolution of a few centimeters along the strip and a sufficient timing performance for rejecting background hits and hadronic showers.
- The hit occupancy is very low. Thus, the detector segmentation is constrained by the electronics cost and the spatial resolution for matching MTD hits with the projected TPC tracks. This projection resolution is momentum dependent and is about 6 cm.
- The system must be installed outside the magnetic return yokes ("backlegs"), and the BEMC PMT boxes, which are already mounted on the backlegs. The mechanics needed for mounting the MTD system on this PMT boxes must be modular and capable of allowing individual MTD boxes to be easily replaced and also allow convenient access to the BEMC PMT boxes.
- The system must be able to operate in the fringe field from the 0.5T STAR magnetic field.
- The system must be able to operate with low noise rates. The MTD must be capable of sufficiently selective triggering on di-muon pairs. To insure that the random trigger rates due to the LMRPC noise is low compared to the expected rates of the di-muon triggers, the total noise rate should be <100 kHz.
- The system must be safe, and meet all BNL safety requirements.
- The system must not impair the performance of other STAR detectors. This concerns the effects of the ease of access to the BEMC PMT boxes for maintenance, and various interactions with the TOF system. The MTD group will work with BEMC group and operation team to have a final design on the supporting structures for the MTD trays. The discussion is currently on-going and the detailed documentation can be found elsewhere [51]. The MTD R&D proposal has been submitted to STAR for year 2011, which can be found at Ref. [52].

We have proposed a cost-effective and compact muon telescope detector using the MRPC technology with long strips. This design has a sufficient time resolution and is impervious to magnetic fields. It is also inexpensive, reliable, and relatively easy to construct. Most of the authors of the present proposal participated directly in the development of this technology at CERN and construction and commissioning of the STAR TOF system. We will use the same electronics, gas system, and HV and low voltage (LV) systems as the STAR TOF. In addition, we obtained a BNL Laboratory directed R&D fund (LDRD 07-007) in 2008–2009 to study the feasibility. We have assembled several prototypes and tested them in STAR, with cosmic rays, and in a Fermilab test beam.

8.2. MRPC module construction

The MRPC technology was first developed by the CERN ALICE group [53]. Recently, this technology was successfully deployed as TOF systems in both STAR and PHENIX. It has proven to be inexpensive, simple to construct, and capable of the necessary timing resolution.

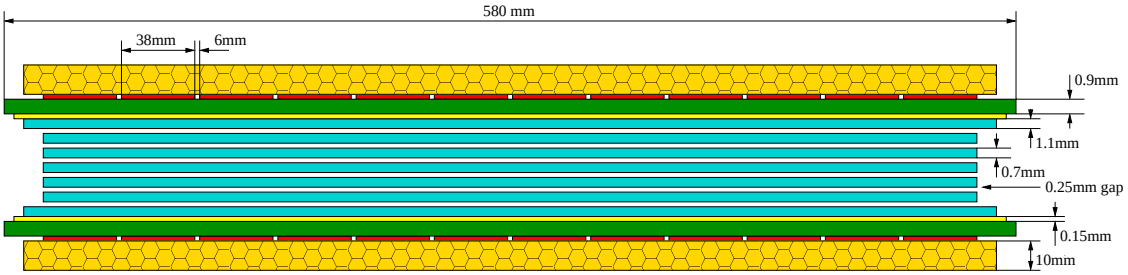

Figure 32. End view of an LMRPC module for the full MTD.

The LMRPC module has six gas gaps arranged in a single stack as shown schematically in Fig. 32. The thickness of each gap is 250 μm and is defined using nylon monofilament fishing line. Float glass sheets of 0.7 mm thickness and a volume resistivity of $\sim 10^{13}$ Ω·cm are used as the resistive plates. The positive and the negative high voltage electrodes are formed with Licron 1756 resistive paint as in the ALICE TOF system. These have a surface resistivity of $\sim$5 M$\Omega/\Box$ and are located outside the outermost "thick" glass layers, which are 1.1 mm thick. The active area of each LMRPC, defined by the inner glass stack, is 89 cm $\times$ 52 cm^2. The read-out pads are segmented into 12 double-ended strips which are 3.8 cm wide. There is a 6 mm gap between each strip. Twisted-pair cables bring the differential signals from each end of each strip to the front-end electronics. The LMRPC modules are enclosed in a gas-tight aluminum box that is filled with a mixture of 95% Freon R-134a and 5% iso-butane.

8.3. Tray Assembly and Mounting Structure

The primary mechanical structure of the MTD system is a "tray". Each is a simple aluminum box built using off-the-shelf raw materials. Each tray holds the detectors in three dimensions at a specific position in STAR, provides the mount points for the on-detector electronics, and forms the leakless gas volume. The proposed MTD trays are considerably simpler than those built for the STAR TOF system and the Run-7 and Run-9 MTD prototypes.

An exploded view of a tray is shown in Fig. 33. Each consists of three basic components which are now described going from the bottom to the top of this figure.

- **Body** – This is formed using 1 inch $\times$1.5 inch architectural aluminum channel spot welded to a 1/8 inch thick aluminum sheet. Dow-Corning DC730 freon resistant sealant is applied to all inner corners. The gas and HV feedthroughs mount to the body via holes in the web of the channel. Delrin spacers are used to stand-off the LMRPC from the edges of the body. Plates spot-welded to the wings of the channel provide the

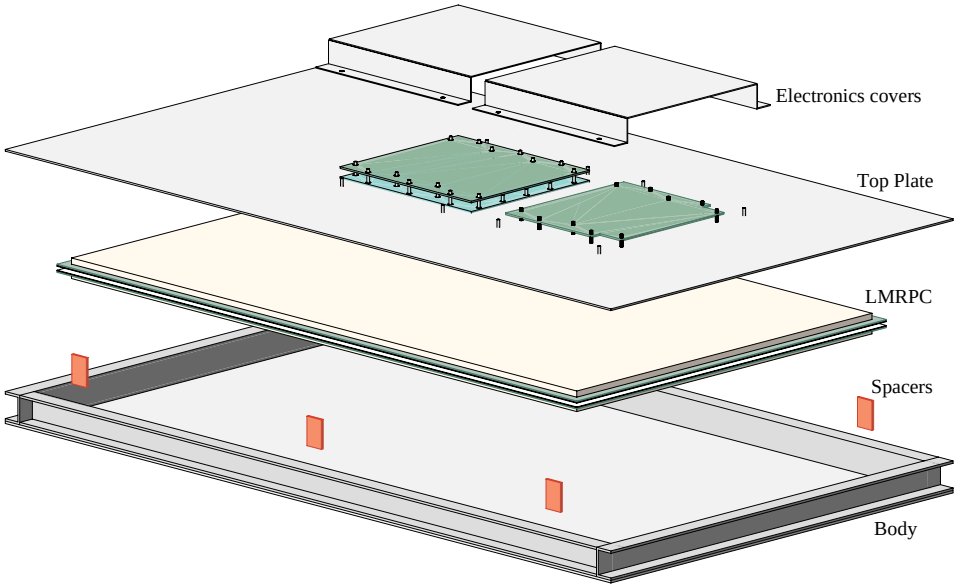

Figure 33. An exploded view of an MTD tray.

mount points to the unistrut support structure that attaches to the BEMC PMT boxes (not shown). This support structure will be similar to that used for the Run-9 MTD prototype and is shown in the left frame of Fig. 34.

- **Top** – This is a 0.090 inch thick aluminum sheet that includes a large hole in the center to allow the connection of the LMRPC signal pigtails to the electronics and a number of PEM studs for the attachment of the electronics. The top is bolted to the upper wings of the body channel and edge-sealed using DC-730 sealant.
- **Covers** – These are 0.050 inch thick aluminum and protect the electronics mounted to the tray top.

Shown on the right side of Fig. 34 is a view of four magnet backlegs, the BEMC PMT boxes, and the five MTD trays per backleg. There are a total of 30 backlegs and 117 MTD trays in the system in total. There are 3 backlegs without any MTD tray. For the bottom 9 backlegs, there are 3 trays in each backleg; for the other 18 backlegs, there are 5 trays in each backleg. Each backleg includes one tray with a TCPU board. The other four or two trays on each backleg do not have TCPU boards. As described in the next section, the TCPU boards collect the information from the TDIG boards and delivers it to the THUB data collectors. Thus, the TDIG boards from a group of five or three trays on each backleg are connected to one TCPU.

The MTD detectors are mounted on the exterior of STAR (not inside the magnet as for STAR TOF), and there are much fewer electronics boards per tray and in total. Therefore a water cooling system for the MTD system is not expected to be necessary. The electronics covers are open on two opposite sides which will allow a sufficient amount of heat removal

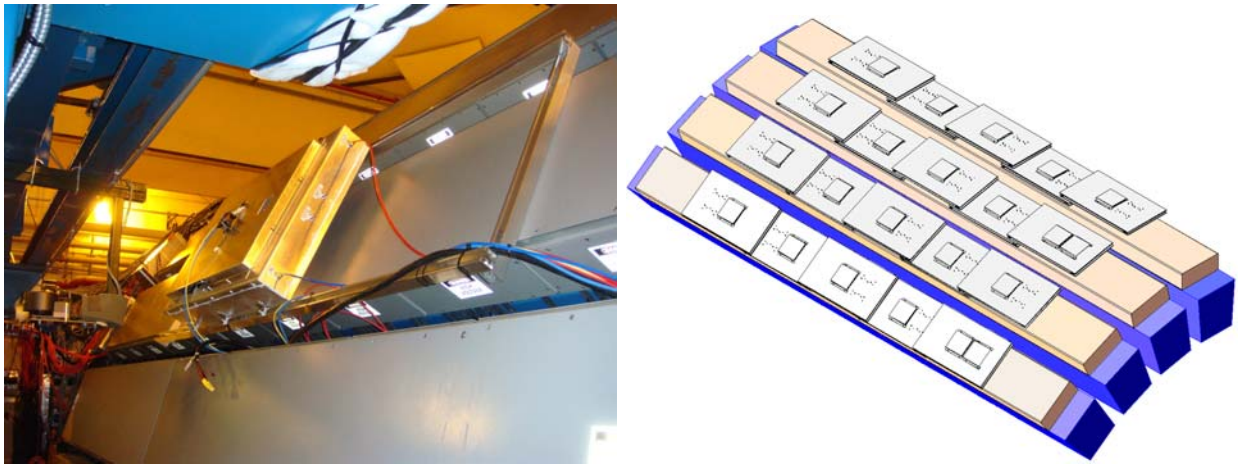

Figure 34. On the left is the MTD prototype and its support structure in year 2009, and on the right is a conceptual view of four magnet backlegs, the BEMC PMT boxes on each backleg, and the 5 MTD trays that mount to each BEMC PMT box.

via unforced air convection. Each MTD tray draws less than 20 W.

8.4. Readout Electronics

The readout electronics for the MTD are very similar as those used in the STAR TOF system. Each tray consists of one LMRPC module with 24 read-out channels. The MTD electronics record the time of signals in the LMRPC detectors and deliver the information to the STAR Data AcQuisition (DAQ) system. It also provides analog multiplicity information from each end of each LRMPC to the STAR Level-0 trigger for discriminating and timing measurements at the trigger level.

The key chips ("NINO" and "HPTDC") were developed at CERN for the ALICE TOF system. The electronics boards that use these chips ("TINO" and "TDIG") were developed for the STAR TOF system by Rice University and Blue Sky Electronics, respectively. The primary data collector boards, "TCPU" and "THUB," were developed at Blue Sky electronics, and UT-Austin, respectively, whle the trigger interface board, "TTRG," was developed at Rice. Additional details on these boards are presented in this section and are also available in the STAR TOF proposal [7].

The electronics required for this system are as follows.

- **TINO4** – The TINO4 card is the interface between each LMRPC and a TDIG digitization card. Each TINO4 card accepts the 24 signals from the two ends of each LMRPC. The TINO4 card amplifies and discriminates the LMRPC signals using the ALICE NINO analog ASIC. There are 117 TINO4 cards in total. This card is very similar but not exactly the same as that used in the STAR TOF system. The MTD requires an analog multiplicity signal from each end of each LMRPC separately in order to allow low-level triggers on the strip mean-times and time-differences along the strips.

This is not possible with the TOF version of the TINO board. The TINO4 board includes 4 NINO chips (instead of the 3 NINOs on TOF's TINO) in order to provide the required information for the MTD triggering.

- **TTRG** – In the Run-9 MTD prototype (as well as the Run-8 STAR TOF trays), the (very simple) TTRG board collected the multiplicity signals from the NINO chips and formed analog signals for triggering. In order to preserve the capability for triggering on both the LMRPC mean times and strip time differences, two TTRG boards per backleg are used - one TTRG collects the multiplicity information from one end of each of the 5×12 or 3×12 strips, and the other TTRG collects the multiplicity information from the other end of the strips in these five or three LMRPCs. There are thus 54 TTRG boards in total.
- **TDIG** – The TDIG card receives the discriminated signals from the TINO4 board and performs the time digitization using the HPTDC chip. The TDIG boards for the MTD system are exactly the same as those in use in the STAR TOF system. There are thus 117 TDIG boards in total.
- **TCPU** – The TCPU card concentrates the data from the five or three trays on the same backleg (five or three TDIG cards) and sends it to the THUB data collector boards. The TCPU boards also distribute the 40 MHz master clock to each TDIG board. There are 27 TCPU cards in total.
- **THUB** – A THUB board collects the information from a number of TCPU boards and sends it to the STAR DAQ system via a CERN/ALICE SIU daughter card and optical fibers. A THUB board also defines and distributes the low-jitter 40 MHz master clock signal for the whole system. There are two THUB boards in the MTD system, one near the top of STAR and one near the bottom, and each collects the information from fourteen or thirteen TCPU boards. Each THUB board is installed inside a protective chassis that is mounted to the magnet steel as in the STAR TOF system.
- **DAQ Receiver** – The MTD DAQ receiver is a Linux-based personal computer with a PCI based CERN/ALICE D-RORC optical interface and a Myrinet interface.

The following deliverables are involved in implementing the electronics subsystem:

- electronics board purchase and board testing;
- electronics integration and system testing: engineering redesign, firmware debugging and modification;
- electronics installation and commissioning;
- electronics configuration and calibration software and control software;
- low-voltage systems;

The electronics board purchase and testing will be managed at Rice University. The low voltage systems will use the same Wiener supplies as used in the STAR TOF system. The purchase of the LV power supplies will be managed by BNL.

The TIN04 and TDIG cards are mounted to the detector trays as part of the assembly process at UT. A TCPU board is installed on one tray (near η=0) on each backleg, and this TCPU card controls the five or three TDIG boards on this same backleg. The trays are then tested at UT as complete detector units including the integrated on-board read-out electronics. The trays are shipped to BNL as complete detector units including the electronics. The installation at BNL will include the mechanical installation of the trays on the BEMC PMT boxes outside the magnet backlegs and the various ancillary connections (HV, gas, and cabling). The electronics installation includes the connections to the STAR Trigger, THUB boards, the low and high voltage supplies, and the fiber connection from the THUB boards to the STAR DAQ. The electronics commissioning of the detector consists integrating the detector electronics into the STAR trigger and DAQ systems.

8.5. Integration and Operation

The fundamental aspects of the MTD design and read-out electronics are identical to that successfully deployed in the STAR TOF system. We will be able to use the same model high- and low-voltage supplies, and the same interfaces to the STAR slow controls for monitoring and safety alarms. The gas system is a closed circulation system with purification, and the MTD trays will be treated as additional TOF trays. The integration space at platforms for the MTD system will be less than two rack space.

The MTD trigger crate is available now and additional four QT boards are required. The QT boards have been used in the STAR trigger system for many detectors: the Beam Beam Counters, Forward Meson Spectrometer, Zero-Degree Calorimeters, and Vertex Position Detector. These boards are used as ADCs, TACs, and as the first layer of the trigger decision tree. All these components and integration have been installed and tested successfully in Run-9 with a prototype MTD.

8.6. Project Cost-Schedule and Resources

The cost of the LMRPC MTD barrel construction is proposed to be shared jointly by the U.S. and Chinese institutions collaborating on the project. The U.S. part of the construction project is projected to be \$1.4M in FY2009 dollars, adjusted for inflation over the life of the project. The proposed Chinese contribution in equivalent U.S. dollars is valued at \$0.5M dollars. A budget for the proposal is shown in Fig. 35. Contingency has been estimated for all costs and included as a separate column. Overhead of 50% is included for labor costs. Overhead is included elsewhere as applicable..

The project schedule is shown in Fig. 36. The construction schedule begins in the first quarter of FY2011. Long MRPC module construction in China would begin at this time and continue until the second quarter of FY2012. The construction of the mechanical and electronic components would also begin at the end of FY2010, allowing for installation of a 2-tray system in time for Run-11. Detector construction and commissioning would be

completed by the end of FY2013.

The team within STAR proposing to construct and integrate this detector system consists of 47 scientists, engineers, and students from 10 institutions in the United States (4), China (6) and India (1). Figure 37 lists the manpower and institution responsibilities.

In addition to contributing to the scientific measurements afforded by this detector system, the Chinese institutions will be responsible for providing high quality MRPC modules, built and tested in China, for integration into the barrel MTD system. These groups have extensive experience with this technology from having successfully installed and commissioned the TOF system in STAR. The prototype LMRPC modules constructed in China were installed in the prototype MTD tray and were tested at the Fermilab test beam (T963), and operated successfully in STAR in RHIC Runs 7-9. The results of these tests indicate the LMRPC MTD detectors that were tested meet all STAR specifications. In addition, VECC (India) will contribute a small amount of MRPC modules.

The U.S. institutions participating in this project are responsible for the design, fabrication, testing, and integration of the front-end and read-out electronics as well as the mechanical assemblies required for this detector. They are responsible as well for overall project management and coordination.

The proposed MTD upgrade is another important STAR construction project involving international cooperation, with the STAR groups from China contributing significantly to the project both financially and technically. This project has been discussed in concept with the Directorate of the National Natural Science Foundation of China, which looks forward to reviewing a corresponding Chinese proposal once the review process for this proposal is begun by the U.S. Department of Energy. The team proposing to construct this detector has considerable experience in TOF techniques, in MRPC construction and testing, and in high energy and nuclear physics experiments in general.

References

[1] L. Ruan *et al.*, J. Phys. G **36**, 095001 (2009).
[2] J. Adams *et al.*, Nucl. Phys. A **757**, 102 (2005).
[3] I. Arsene *et al.*, Nucl. Phys. A **757**, 1 (2005); K. Adcox *et al.*, Nucl. Phys. A **757**, 184 (2005); B.B. Back *et al.*, Nucl. Phys. A **757**, 28 (2005).
[4] R. Rapp and J. Wambach, Adv. Nucl. Phys. 25 (2000) 1.
[5] Electromagnetic Probes at RHIC II (Working Group Report), G. David, R. Rapp and Z. Xu, Phys. Rept. **462**, 176 (2008).
[6] Z. Xu, BNL LDRD project 07-007; Beam Test Experiment (T963) at FermiLab.
[7] STAR Time-of-Flight Proposal: http://www.star.bnl.gov/STAR/tof/publications/TOF_20040524.pdf.
[8] A. D. Frawley, T. Ullrich and R. Vogt, Phys. Rept. **462**, 125 (2008).
[9] T. Matsui and H. Satz, Phys. Lett. **B178**, 416 (1986).
[10] M. C. Abreu et al., Phys. Lett. **B499**, 85 (2001).
[11] X. Zhao and R. Rapp, Phys. Lett. **B664**, 253 (2008).
[12] J. P. Blaizot and J.-Y. Ollitrault, Phys. Rev. **D39**, 232 (1989).
[13] F. Karsch and R. Petronzio, Phys. Lett. **B212**, 255 (1988).

MTD system	Cost	Contin.	Sum	FY11	FY12	FY13
Detectors and Mechanical Systems						
Tray						
Tray supplies	6852	2261	9113			
Tray parts	37360	9340	46700			
Fabrication	9740	3409	13149			
Mounting Structure	6552	2293	8845			
Fixture	11000	3850	14850			
Shipping	12200	1220	13420			
Travel	28200	2820	31020			
Technician	88000	8800	96800			
Tray (labor)	88000	8800	96800	48400	48400	
Tray (total)	199904	33993	233897	116949	116949	
Gas System						
Mass flow controller	6000	600	6600			
gas distribution	2000	200	2200			
Travel	5000	500	5500			
Gas System	13000	1300	14300	14300		
High voltage system						
Distribution	97000	9700	106700	53350	53350	
Supplies	37000	3700	40700	40700		
High voltage system	134000	13400	147400	94050	53350	
Detector and Mechanical ... (labor)	88000	8800	96800	48400	48400	
Detectors and Mechanical ... (total)	346904	48693	395597	225299	170299	
Electronics						
Electronics board purchase, testing, installation and integration						
TINO4	39000	7800	46800			
TDIG	198000	19800	217800			
TCPU	42000	4200	46200			
THUB	20000	4000	24000			
TSER	5000	1000	6000			
TTRG	17000	3400	20400			
TOSC	24000	4800	28800			
HPTDC	24000	2400	26400			
DRORC/SIU	8000	800	8800			
Board cost	*377000*	*48200*	*425200*			
Connection/cables	25000	5000	30000			
Engineering design, installation, and integration	278000	55600	333600			
MSTC	72000	7200	79200			
Electronics board purchase, ... (labor)	278000	55600	333600	166800	166800	
Electronics board purchase, ... (total)	752000	116000	868000	434000	434000	
Low voltage system						
Power supplies	27000	2700	29700			
cables	8000	800	8800			
Low voltage system	35000	3500	38500	19250	19250	
Trigger QT boards	60000	6000	66000	66000		
Electronics (labor)	278000	116000	333600	166800	166800	
Electronics (total)	847000	125500	972500	519250	453250	
Sum (labor)	366000	64400	430400	215200	215200	
Sum (total)	1193904	174193	1368097	744549	623549	

Figure 35. The cost estimation for the MTD systems with 117 trays. Contingency has been estimated for all costs and included as a separate column. Overhead of 50% is included for labor costs. Overhead is included elsewhere as applicable. There is no overhead added to equipment costs at UT and Rice.

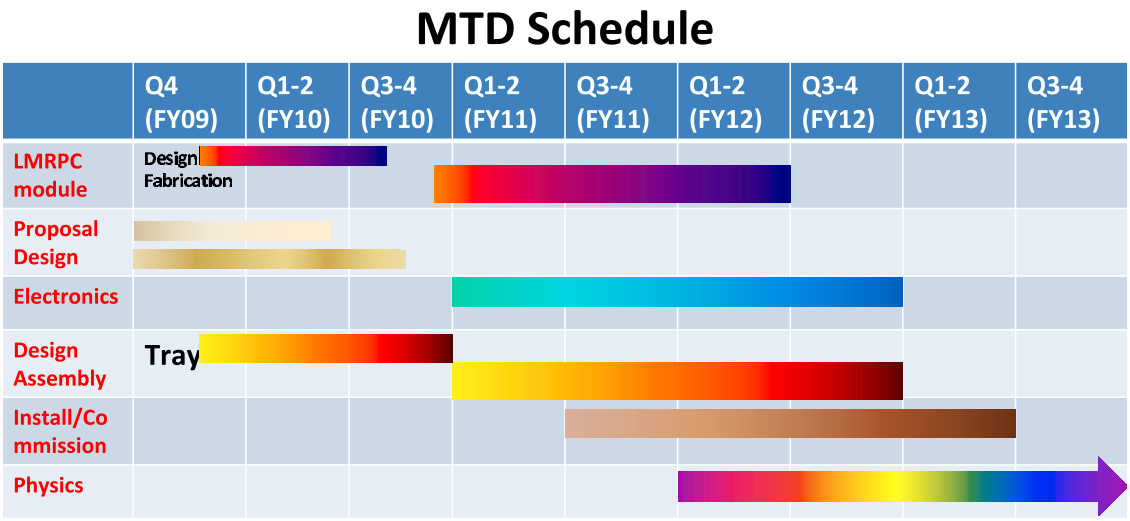

Figure 36. MTD schedule for the fabrication of the LMRPC modules in China, the electronics, as well as the tray assembly and installations and commissioning. The project completes at the end of Q4 of FY13.

Institutional Responsibilities

Institute	Responsibilities	Manpower, Expertise
BNL	Commission, Proposal, Management, Calibration	4 staff + 2 students
Rice	Electronics, Tray design, Integration	4 + 2 EE + 2 students TOF
Texas Austin	Tray Fabrication and Test	3 + 2 students + technical staff TOF
Texas A&M	Simulations, Physics Case	1 + 1 student Hard Probes
UC Davis	L2 trigger	1 + 1 Heavy-Flavor
UC Berkeley	QT, L0	2 Trigger
Tsinghua University	LMPRC modules	2 + 1 technician Mass production
USTC	LMRPC modules, Calibration	3 + 2 post + 1student R&D, production
VECC	LMRPC modules, Analyses (in progress)	Detector production

Figure 37. The manpower and institutional responsibilities for the MTD project.

[14] A. Adare et al., Phys. Rev. Lett. **98**, 232301 (2007a).
[15] P. Braun-Munzinger and J. Stachel, Phys. Lett. **B490**, 196 (2000).
[16] L. Grandchamp and R. Rapp, Phys. Lett. **B523**, 60 (2001).
[17] M. I. Gorenstein et al., Phys. Lett. **B524**, 265 (2002).
[18] R. L. Thews, M. Schroedter, and J. Rafelski, Phys. Rev. **C63**, 054905 (2001).
[19] H. Liu, K. Rajagopal, and U.A.Wiedemann, Phys. Rev. Lett. **98**, 182301 (2007).
[20] C. Adler et al., Phys. Rev. Lett. **89**, 202301 (2002).
[21] A. Adare et al., Phys. Rev. Lett. **101**, 122301 (2008).
[22] A. Adare et al., Phys. Rev. Lett. **98**, 232002 (2007c).
[23] T. Gunji et al., J. Phys.G: Nucl. Part. Phys. **35**, 104137 (2008).
[24] R. Vogt, M. Cacciari and P. Nason, Nucl. Phys. A 774 (2006) 661.
[25] H. Satz, J. Phys. G **32**, R25 (2006).
[26] H. van Hees and R. Rapp, Nucl. Phys. A **806**, 339 (2008).
[27] R. Arnaldi *et al.*, Phys. Rev. Lett. **100**, 022302 (2008).
[28] R. Arnaldi *et al.*, Phys. Rev. Lett. **102**, 222301 (2009).
[29] K. H. Ackermann *et al.*, Nucl. Instr. Meth. A **499**, 624 (2003).
[30] M. Anderson *et al.*, Nucl. Instr. Meth. A **499**, 659 (2003).
[31] M. Shao *et al.*, Nucl. Instr. Meth. A **558**, 419 (2006).
[32] H. Bichsel, Nucl. Instr. Meth. A **562**, 154 (2006).
[33] Y. Xu *et al.*, 0807.4303.
[34] B. Bonner *et al.*, Nucl. Instr. Meth. A **508**, 181 (2003); M. Shao *et al.*, Nucl. Instr. Meth. A **492**, 344 (2002); J. Wu *et al.*, Nucl. Instr. Meth. A **538**, 243 (2005).
[35] J. Adams *et al.*, Phys. Lett. B **616**, 8 (2005).
[36] M. Beddo *et al.*, Nucl. Instr. Meth. A **499**, 725 (2003).
[37] F. Bergsma *et al.*, Nucl. Instr. Meth. A **499**, 633 (2003).
[38] G. Lin for the STAR Collaboration, A New Large-area Muon Telescope Detector at Mid-rapidity at RHIC, talk presented at DNP 2006, Nashville, TN, Oct. 25-28.
[39] Z. Tang for the STAR Collaboration, contribution to QM2008 proceedings, arXiv:0804.4846, J. Phys. G **35**, 104135 (2008); B.I. Abelev *et al.*, Phys. Rev. C **80**, 041902 (2009), arXiv:0904.0439.
[40] Z. Tang, Ph.D. thesis, University of Science and Technology of China (2009).
[41] S.S. Adler *et al.*, Phys. Rev. C **69**, 014901 (2004).
[42] F. Jin for the STAR Collaboration, contribution to SQM2008 proceedings, arXiv:0901.0693.
[43] D. Acosta *et al.*, Phys. Rev. Lett. **88**, 161802 (2002).
[44] G. Moreno *et al.*, Phys. Rev. D **43**, 2815 (1991); L. Y. Zhu *et al.*, Phys. Rev. Lett. **100**, 062301 (2008).
[45] Y. Sun et al., Nucl. Instr. Meth. A **593**, 307 (2008).
[46] W.J. Llope *et al.*, Nucl. Instr. Meth. A **596**, 430 (2008).
[47] F. S. Bieser *et al.*, Nucl. Instr. Meth. A **499**, 766 (2003).
[48] S. Eidelman *et al.*, Phys. Lett. B **592**, 1 (2004).
[49] W.J. Llope *et al.*, Nucl. Instr. Meth. A **522**, 252 (2004).
[50] J. Adams *et al.*, Phys. Rev. Lett. **94**, 62301 (2005); B.I. Abelev *et al.*, Phys. Rev. Lett. **98**, 192301 (2007).
[51] MTD design and integration summary, December 2009, http://wjllope.rice.edu/∼MTD/MTDintegration.pdf.
[52] STAR MTD R&D proposal for year 2011, submitted to STAR.
[53] E. Cerron Zeballos *et al.*, Nucl. Instr. Meth. A **374**, 132 (1996); M.C.S. Williams *et al.*, Nucl. Instr. Meth. A **478**, 183 (2002).